

^{12}CO OBSERVATIONS OF THE MOLECULAR
CLOUD ENCOMPASSING SHARPLESS 222 (LK H α 101)

by

RICHARD ALLAN CHRISTIE

B.Sc., The University of British Columbia, 1978

A THESIS SUBMITTED IN PARTIAL FULFILMENT OF
THE REQUIREMENTS FOR THE DEGREE OF
MASTER OF SCIENCE

in

THE FACULTY OF GRADUATE STUDIES
DEPARTMENT OF PHYSICS

We accept this thesis as conforming
to the required standard

THE UNIVERSITY OF BRITISH COLUMBIA

August 1981

© Richard Allan Christie, 1981

In presenting this thesis in partial fulfilment of the requirements for an advanced degree at the University of British Columbia, I agree that the Library shall make it freely available for reference and study. I further agree that permission for extensive copying of this thesis for scholarly purposes may be granted by the head of my department or by his or her representatives. It is understood that copying or publication of this thesis for financial gain shall not be allowed without my written permission.

Department of PHYSICS

The University of British Columbia
2075 Wesbrook Place
Vancouver, Canada
V6T 1W5

Date Aug 15 / 81

ABSTRACT

The 4.57 meter millimetre wave telescope at the University of British Columbia has been used to partially map a region around Lk H α 101 one half degree in diameter centered on $\alpha(1950) = 04^{\text{h}}26^{\text{m}}34^{\text{s}}.0$ (right ascension), $\delta(1950) = 35^{\circ}13'00''$ (declination) in the $J=1 \rightarrow 0$ transition of $^{12}\text{C}^{16}\text{O}$.

Our ^{12}CO results show a wide region of ^{12}CO emission, but the exact boundaries are as yet undetermined. The north and west boundaries have been determined. We suspect the emission extends as far as a visual extinction of 1 magnitude which covers a region almost one degree across and several degrees long. The average radiation temperature, T_{A}^* , is 10 K. Within our survey field we found a large fragmented area with five hot spots (20 K).

Since ^{13}CO observations were not made ^{13}CO data was generated from the ^{12}CO observations. Both the ^{12}CO and ^{13}CO temperature contours have five hot spots within a single envelope of colder CO emission located southeast of Lk H α 101. Three CO clouds (#1, #2, and #3) are resolved at Lk H α 101 (7.2, -10.8), Lk H α 101 (0.0, -10.8), and Lk H α 101 (7.2, -5.4). Their masses were calculated from the generated ^{13}CO column densities and are $49M_{\odot}$, $41M_{\odot}$, and $25M_{\odot}$ respectively. Two other clouds (#4 and #5) on the limit of resolution are located at Lk H α 101 (3.6, -5.4) and Lk H α 101 (0.0, -1.8) and have masses of $11M_{\odot}$ and $25M_{\odot}$. Each of these fragments is embedded in the same 13 K ^{12}CO contour centered on Lk H α 101 (3.6, -7.2). The mass is calculated from the fabricated ^{13}CO data and should not be relied upon very strongly. It is in error by at most a factor of

two.

Peak HI emission contours (Dewdney and Roger 1981) are anticorrelated to our peak CO contours. The HI lies to the northwest. This indicates that the peak CO and HI features are located in different regions. The peak HI column densities derived from both the fabricated ^{13}CO data and HI observations agree. They are $\sim 1.3 \times 10^{21}$ atoms cm^{-2} .

From star counts we made of the region we see that the stronger CO emission correlates with regions of stronger visual extinction. The peak HI occurs where the extinction is low. The exciting star has presumably been able to dissociate H_2 into HI to the northwest where the visual extinction is lower. Dewdney and Roger (1981) have modelled this asymmetry reasonably well by assuming there is a steep discontinuity of density near Lk H α 101 to the east.

The positions of infrared stars from the Steward Observatory Near Infrared Photographic Sky Survey provide meager evidence for the 'Blister' model (Israel 1977, Gilmore 1978) and suggest that star formation was initiated on the edge of the cloud and proceeded inwards. Our CO hot spots could well be the next generation of infrared stars. Confirmation will require a more complete map with better resolution of the region around Lk H α 101 (3.6, -7.2).

TABLE OF CONTENTS

| | |
|--|-----|
| Abstract | ii |
| Table Of Contents | iv |
| List Of Figures | v |
| List Of Tables | vi |
| Acknowledgements | vii |
| I. INTRODUCTION | 1 |
| II. DATA ACQUISITION | 6 |
| II.1-Site | 6 |
| II.2-Equipment | 7 |
| II.3-Observing Sequence | 10 |
| II.4-On-Site Data Handling | 19 |
| III. DATA REDUCTION AND ANALYSIS | 21 |
| III.1-Calibration | 21 |
| III.2-Representation Of Lk HX101 Through Global Plots ... | 31 |
| III.3- ^{12}CO Radiation Temperatures | 36 |
| III.4-Generating Model For ^{13}CO | 41 |
| III.5-Generated ^{13}CO Column Densities | 48 |
| III.6-Star Counting Theory, Data And Results | 55 |
| IV. DISCUSSION OF RESULTS | 71 |
| IV.1.1-Previous Observations: Introduction | 71 |
| IV.1.2-Previous Observations: HI Results | 78 |
| IV.1.3-Previous Observations: CO Results | 83 |
| IV.2-Our Observations | 86 |
| V. CONCLUSIONS | 103 |
| Bibliography | 105 |
| Appendix: T_A^* (^{12}CO) Contours At Constant Velocity | 108 |

LIST OF FIGURES

| | |
|--|-----|
| Figure 1-The Receiver | 9 |
| Figure 2-Reference Position Spectrum | 18 |
| Figure 3-Lk H α 101 (5.4,-3.6)-Tipping Curve Calibration | 28 |
| Figure 4-Lk H α 101 (5.4,-3.6)-OMC1(Orion A) Calibration | 30 |
| Figure 5-Global Plot (Tipping Curve Calibration) | 33 |
| Figure 6-Global Plot (OMC1(Orion A) Calibration) | 35 |
| Figure 7-Integrated ^{12}CO Contours | 40 |
| Figure 8- T_A^* (^{13}CO) Vs. T_A^* (^{12}CO)/ T_A^* (^{13}CO) Ratios | 45 |
| Figure 9-Generated T_A^* (^{13}CO) Contours | 47 |
| Figure 10-Generated N_{col} (^{13}CO) Contours | 54 |
| Figure 11- A_B Extinction Contours | 63 |
| Figure 12- A_R Extinction Contours | 64 |
| Figure 13- A_V Extinction Contours | 65 |
| Figure 14-Infrared Diagram | 77 |
| Figure 15-HI Contour Map, Felli And Churchwell (1972) | 80 |
| Figure 16-HI Profile, Dewdney And Roger (1981) | 81 |
| Figure 17-3-D Display Of HI Results | 82 |
| Figure 18- ^{12}CO Profile Dip | 85 |
| Figure 19-Comparison Of ^{12}CO , HI, A_V Etc. | 102 |
| NOTE: SIX OVERLAYS OF THE RESULTS FOR FIGURE 19in pocket | |

LIST OF TABLES

| | |
|---|-----|
| Table I-Observation Details | 14 |
| Table II- T_A^* (^{13}CO) Generating Model | 44 |
| Table III-Profile Half Width Ratios | 51 |
| Table IV-Velocity Calculations | 52 |
| Table V-Van Rhijn's Table For $b = -9.0^\circ$ | 61 |
| Table VI-Data Summary | 67 |
| Table VII-Infrared Star Positions | 75 |
| Table VIII-Peak N_{col} (^{13}CO) And Related A_V | 98 |
| Table IX-Virial Cloud Masses | 99 |
| Table X- N_{col} (^{13}CO) Cloud Masses | 100 |

ACKNOWLEDGEMENTS

I wish to thank my thesis supervisor, Dr. W.H. McCutcheon, for his continued encouragement and suggestions during the course of this project.

I thank the other members of our group, Dr. W.L.H. Shuter and Mr. C.P. Chan for their valued contributions.

Finally, I would like to thank three groups for their generous contribution of unpublished data on Sharpless regions: Drs. P. Dewdney and R. Roger at the Dominion Radio Astrophysical Observatory (D.R.A.O.), for their Sharpless 222 HI results, Dr. E. Craine of the Steward Observatory, for sending a print of Sharpless 222 from their infrared sky survey and Dr. P. Jackson of the University of Maryland for sending a copy of J. Sewall's second year project covering ^{12}CO and ^{13}CO observations for three Sharpless regions.

I. INTRODUCTION

The $J=1 \rightarrow 0$ transition of interstellar $^{12}\text{C}^{16}\text{O}$ was first detected by Wilson et al. (1970). Penzias et al. (1971) found that CO column densities are systematically higher near HII regions. It is now accepted that CO emission, along with emission from other molecules and maser line emission, are often indicators of recent star formation.

The use of CO emission as a probe of interstellar molecular clouds was recognized at once. CO is the most abundant interstellar radio molecule, and its relatively long lifetime means that the $J=1$ level can be populated even in regions with small excitation rates. Penzias et al. (1972) showed that this level could be well populated in typical molecular clouds through collisions between CO and neutral hydrogen molecules. They also found that if the $J=1 \rightarrow 0$ transition was optically thick in a uniformly dense cloud, thermalization of the transition would be assured by the radiative trapping of the $J=1 \rightarrow 0$ photons.

Wherever the $J=1 \rightarrow 0$ transition for ^{12}CO has been detected it has been found to be optically thick and hence it can be used to determine the kinetic temperature. ^{13}CO is not usually saturated since it is far less abundant than ^{12}CO . As a result, ^{13}CO is generally used as a density probe. In some cases even ^{13}CO has a high optical depth (Sewall 1980). For this reason it would be better to use the even less abundant $^{12}\text{C}^{18}\text{O}$ isotope for probing dense cloud centres.

The cause of the observed CO line widths has sparked considerable controversy. The thermal line width, assuming

typical parameters for a molecular cloud, is about 0.1 km s^{-1} . Observations indicate line widths many times larger. Generally, these line widths would correspond to supersonic dispersion velocities. If the line widths are caused by turbulent motions, tremendous sources of energy are required to prevent rapid damping. Goldreich and Kwan (1974) proposed that the line widths are due to systematic, rather than turbulent, motions. Since the line profiles of different isotopic species generally have similar appearances and show analogous variations throughout the cloud, they argued that the clouds are undergoing some systematic motion such as gravitational collapse. Goldreich and Kwan (1974) found that the clouds cooled faster by CO emission than they could be heated by adiabatic compression and the release of gravitational energy. For very warm clouds ($T_k \gtrsim 25 \text{ K}$) the temperatures implied by the CO line intensities could be maintained by collisions between the gas molecules and the dust grains heated by buried protostars. The frequent association of CO emission with strong infrared point sources is evidence in favor of this model. The large velocity gradient model accounts for most CO line shapes, but there are some strong opposing arguments. These are summarized by Zuckerman and Palmer (1974). We will discuss one of these arguments more fully in section IV.3. To obtain a more detailed description of star formation one needs to incorporate complicated hydrodynamic processes such as turbulence, clumping, and eddies in cloud models.

When CO and H α velocities near an HII region are available one generally finds the H α velocity to be more negative than the CO velocity. This suggests that ionized material is streaming

away from the neutral material which gives rise to the CO emission. Such observations have led to the 'Blister' model (Israel 1977, Gilmore 1978). In this model OB associations form just inside the surfaces of huge elongated molecular clouds where they give rise to ultracompact HII regions. The star formation process is initiated on one side of the cloud complex and autocatalytically proceeds into the cloud. Compact HII regions are generally found near the edge of clouds. The triggering mechanism for star formation is believed to be the passage of shocks into the neutral clouds. Star formation is perhaps initiated by supernovae and/or spiral density waves. Subsequent generations are formed by the shock waves from the recently generated stars (Elmegreen and Lada 1977). The Champagne model (Tenorio-Tagle 1979) gives similar results using numerical modeling.

Habing and Israel (1979) give the following evolutionary sequence for compact HII regions.

"1. The youngest objects are infrared sources without any HII regions, associated, if at all, only with H_2O masers having simple line profiles. These objects may be identified with accreting stars. ...

2. Slightly older are those objects which are similar, but which in addition show high velocity peaks in the H_2O maser line profiles; these peaks indicate the existence of a significant stellar wind, implying the end of the accretion phase. ...

3. Next are the infrared sources associated with the smallest HII regions (3×10^{16} cm diameter). ... Apparently the HII region has grown sufficiently in size to become visible. Surrounding the HII region is a dense shell that sometimes houses an OH maser source.

4. When the HII region has expanded beyond a diameter of 3×10^{17} cm, the OH maser disappears and a blister-type HII region will soon appear."

Why map ^{12}CO emission in Sharpless 222? The results of previous work, summarized in section IV.1, show Sharpless 222 to be a young, compact HII region with a very strong possibility of ongoing star formation. Recently Dewdney and Roger (1981) have mapped this region in the HI line emission with an angular resolution of 2 arcminutes. In conjunction with their work we decided to map the molecular cloud encompassing Sharpless 222. Generally HI and CO sample different constituents of a region and this would provide additional possibilities for interpretation. The HI and CO observations also have approximately the same spatial and velocity resolution. This would make any comparison between the HI and CO observations more meaningful. As well, the approximate size indicated by the outermost HI contour could be mapped with a beam width of several arcminutes in a reasonable time. In retrospect, the latter was actually a poor assumption. Our observations have shown the extent of the cloud is far greater than we had anticipated. As a result of this and time consuming technical difficulties with the telescope, we had to make a few compromises. First, we had to limit the extent of our observations, so that we have determined only 60 per cent of the cloud's edge. Secondly, we could only partially sample much of the observation field. Nevertheless, Sharpless 222 has been a particularly profitable source to examine. It has yielded many interesting phenomena and appears to be prototypic of molecular clouds engaged in star formation.

For the purpose of this project the name Sharpless 222 is used to describe the molecular cloud encompassing the HII

region, NGC 1579, while Lk H α 101 denotes the associated source of the illumination. The one exception is the use of LH101 to label plots and tables.

II. DATA ACQUISITION

II.1-Site

Observations of the Sharpless 222 region were carried out using the 4.57 meter millimetre wave telescope located on the University of British Columbia campus in Vancouver (Shuter and McCutcheon 1974, Mahoney 1976). The telescope is situated at $123^{\circ}13'56''$ West longitude, $49^{\circ}15'11''$ North latitude. The elevation is about 50 meters above sea level. Operating at the ^{12}CO frequency of 115.271 GHz, the telescope has an effective beam width of 0.044 degrees. The pointing repeatability of the telescope is ± 0.015 degrees. Source tracking is at worst ± 0.03 degrees which amounts to the half power beam spacing used as our map spacing. The beam efficiency is about 37 per cent.

II.2-Equipment

The receiver uses a single ended mixer with a gallium arsenide Schottky barrier diode. Both the signal mixer and the two stage parametric amplifier are kept cooled to 20 K in a refrigerated dewar at the focus of the telescope. At 115.271 GHz the system noise temperature for these observations averaged 1200 K (SSB). A schematic of the receiver used is given in Figure 1.

Spectra were obtained using a 64 channel filter spectrometer. Each channel is 250 KHz wide. The channel frequencies range from 299.500 MHz to 315.250 MHz.

Spectra were accumulated in a Fabri-Tek signal averager and various forms of reduction could be carried out by a NOVA 1200 minicomputer. The on-site programs were developed by Mahoney (1976). Full details of the on-site data handling are given in section II.4.

Figure 1 -The Receiver

Figure 1 is a schematic diagram of the 80 to 120 GHz cooled receiver at the University of British Columbia. The average system temperature, T_{sys} , is about 900 K (single sideband) under normal operating conditions.

II.3-Observing Sequence

Eighty-nine positions were observed in the Sharpless 222 region, at spacings of 0.03 degrees. The region observed would fill a circle one-half degree in diameter.

Often a specific spectral position will be written as Lk H α 101 (x.x,y.y) where the numbers following Lk H α 101 represent the offsets in right ascension and declination in arcminutes with respect to our nominal centre position;

$$\alpha(1950)=04^{\text{h}}26^{\text{m}}34^{\text{s}}.0 \quad (\text{Right Ascension})$$

$$\delta(1950)=35^{\circ}13'00''.0 \quad (\text{Declination})$$

This centre position was chosen as the approximate centre of the Dewdney and Roger (1981) HI map. As a result, the illuminating star Lk H α 101 is located at Lk H α 101 (5.4,-3.6).

The spectra were obtained by alternating between ON source, S, scans and OFF source, R, or reference scans in a load switched receiver mode. The term scan refers to the process of obtaining a spectrum by integrating on a single fixed beam position for 320 seconds. The purpose of obtaining reference scans is to improve baseline stability and to subtract receiver noise and sky contributions. Careful selection of the reference region is required to obtain a region free of CO emission. After meticulous visual inspection of the Palomar photographic prints we selected $\alpha(1950)=04^{\text{h}}26^{\text{m}}51^{\text{s}}.7$, $\delta(1950)=34^{\circ}10'00''.0$ as our reference position. In the course of this project we have collected almost thirty scans of the reference region. Summation

of these scans indicates there is negligible ^{12}CO signal in the reference region. Generally the ^{12}CO signal in the reference spectrum is added to each of the map positions. This was not done in our case since the maximum $T_A(^{12}\text{CO})$ in the reference was much less than the root mean square (rms) noise of the average profile and can be neglected. The averaged reference spectrum is given in Figure 2.

In order to determine the total amount of integration time necessary to give a suitable signal to noise ratio we used the following observing format. Each spectrum was the sum of four consecutive ON source minus OFF source pairs. We will represent this as follows /SR/SR/SR/SR/. We decided that each map position would require four scans which total 21^m20^s of integration time.

One third of our observing time is spent moving the telescope from one position to another. Of the remaining time, one half is spent on the reference position. It was then decided that a better efficiency for mapping had to be found. Szabo (1980) considered this problem in his thesis. We have followed his recommendations, using the observing sequence //S₁R S₂/S₃R S₄//. Here S₁, S₂, S₃, and S₄ all represent different map positions. This sequence was repeated four times during the observing period to give the total integration time desired. Beam positions using the same reference were kept far apart to minimize the effect of any correlated noise. The one difference between our observing sequence and Szabo's (1980) was that he observed sixteen different positions each night whereas we observed four different positions each four times. Szabo's (1980) method is technically better since he spreads the data

for these positions over four nights and uses the averaged calibration of these same evenings. However, we found no noticeable improvement using his method, and therefore, we chose our sequence since it allows daily on-site averaging of the four spectra.

Each day we mapped Lk H α 101 (5.4, -3.6) and OMC1 (Orion A) as calibration sources to check the accuracy of our relative calibration. OMC1 was observed at the beginning and end of each observing session to check the consistency of the atmospheric attenuation. The sky temperature was monitored to check for variations in opacity. Approximately every half hour the spectrometer was calibrated using the known sky temperature.

It was originally intended to fully map the region around Lk H α 101. As the project proceeded, ^{12}CO emission was found to be more widespread than we had anticipated and it was decided that we could no longer fully sample the entire field of the cloud. The resulting map is given in section III.2. A small region around Lk H α 101 is fully sampled as well as a cross and diagonal strips over a wide extent of the cloud to determine where the ^{12}CO emission decreases.

Table I summarizes the dates, positions and observing sequences used to obtain the spectra. Also included is an indication of the atmospheric attenuation determined from antenna tipping measurements and the receiver system temperature.

Table I -Observation Details

Table I gives a list of the spectral points and the dates they were observed. Also given is the average atmospheric opacity at the beginning and end of each observing session, ($\bar{\tau}$ in nepers) and the system temperature, T_{SYS} (SSB). The centre (0.0,0.0) position is,

$$\alpha(1950) = 04^h 26^m 34.^s 0 \quad (\text{Right Ascension})$$

$$\delta(1950) = 35^{\circ} 13' 00'' 0 \quad (\text{Declination})$$

Table I - Observation Details

| Date day/month | Points | $\tilde{\tau}$ start-end | T_{sys} (SSB) |
|-------------------|--|-----------------------------|--------------------|
| 29/4 | (+5.4, -7.2) (+5.4, +3.6) (+5.4, -5.4) (+5.4, +7.2) | 0.319-0.373 | 1358 |
| 30/4 | (10.8, -3.6) (+3.6, -3.6) (-3.6, -3.6) (-9.0, -3.6) (+0.0, -3.6) | 0.377-0.375 | 1222 |
| 1/5 | (-9.0, +5.4) (-9.0, -1.8) | 0.460-0.456 | 1134 |
| 1&2/5 | (-9.0, 10.8) (-9.0, -10.8) | | |
| 2/5 | (10.8, +0.0) (-1.8, +0.0) (+5.4, +0.0) (-9.0, +0.0) | 0.327-0.311 | 1186 |
| 3/5 | (0.0, -10.8) (+0.0, +0.0) (+0.0, +5.4) (0.0, +10.8) | 0.351-0.273 | 1134 |
| 4/5 | (-5.4, -10.8) (-5.4, +0.0) (-5.4, +5.4) (-5.4, 10.8) | 0.298-0.345 | 988 |
| 4&6/5 | (+5.4, -1.8) (5.4, -10.8) | | |
| 6/5 | (1.8, -10.8) (+1.8, -1.8) (+1.8, +5.4) (+1.8, 10.8) | 0.370-0.330 | 1224 |
| 7/5 | (-1.8, -10.8) (-1.8, -1.8) (-1.8, +5.4) (-1.8, 10.8) | 0.360-0.327 | 1274 |
| 7&10/5 | (+3.6, -5.4) (+3.6, +0.0) | | |

| Date day/month | Points | $\bar{\tau}$ start-end | T_{sys} (SSB) |
|-------------------|--|---------------------------|--------------------|
| 10/5 | (9.0,-10.8) (+9.0,-1.8) (+9.0,+5.4) (9.0,+10.8) | 0.460-0.426 | 1142 |
| 19/6 | (7.2,-10.8) (+7.2,-5.4) (+7.2,+3.6) (7.2,+10.8) | 0.483-0.391 | 1638 |
| 7/7 | (+0.0,-9.0) (+0.0,+9.0) (-7.2,+0.0) (+7.2,+0.0) | 0.532-0.404 | 1342 |
| 8/7 | (+0.0,-7.2) (+0.0,-1.8) (-3.6,+0.0) (+9.0,+0.0) | 0.562-0.482 | 1370 |
| 9/7 | (+0.0,-5.4) (+0.0,+3.6) (-10.8,0.0) (+1.8,+0.0) (+0.0,-1.8) | 0.525-0.482 | 1524 |
| 18/7 | (+0.0,+7.2) (0.0,-12.6) | 0.684-0.491 | 1548 |
| 19/7 | (+9.0,-7.2) (+3.6,-1.8) (+9.0,-5.4) (+3.6,+3.6) (+9.0,-3.6) (+3.6,-7.2) | 0.700-0.530 | 1560 |
| 21/7 | (0.0,-14.4) (0.0,+12.6) (-12.6,0.0) (12.6,+0.0) | 0.682-0.505 | 1434 |
| 12/11 | (+7.2,-7.2) (-3.6,+3.6) (+9.0,-9.0) (-1.8,+1.8) (+7.2,-3.6) (-5.4,-5.4) | 0.503-0.425 | 1574 |

| Date day/month | Points | $\tilde{\nu}$ start-end | T_{sys} (SSB) |
|-------------------|---|----------------------------|--------------------|
| 15/11 | (10.8,-10.8) (-9.0,+9.0) (+7.2,-1.8) (-7.2,-7.2) (+1.8,+1.8) (-9.0,-9.0) | 0.505-0.485 | 1720 |
| 21/11 | (-10.8,-10.8) (+5.4,+5.4) (-7.2,+7.2) (+7.2,+7.2) (-10.8,10.8) (+9.0,+9.0) | 0.500-0.425 | 1870 |

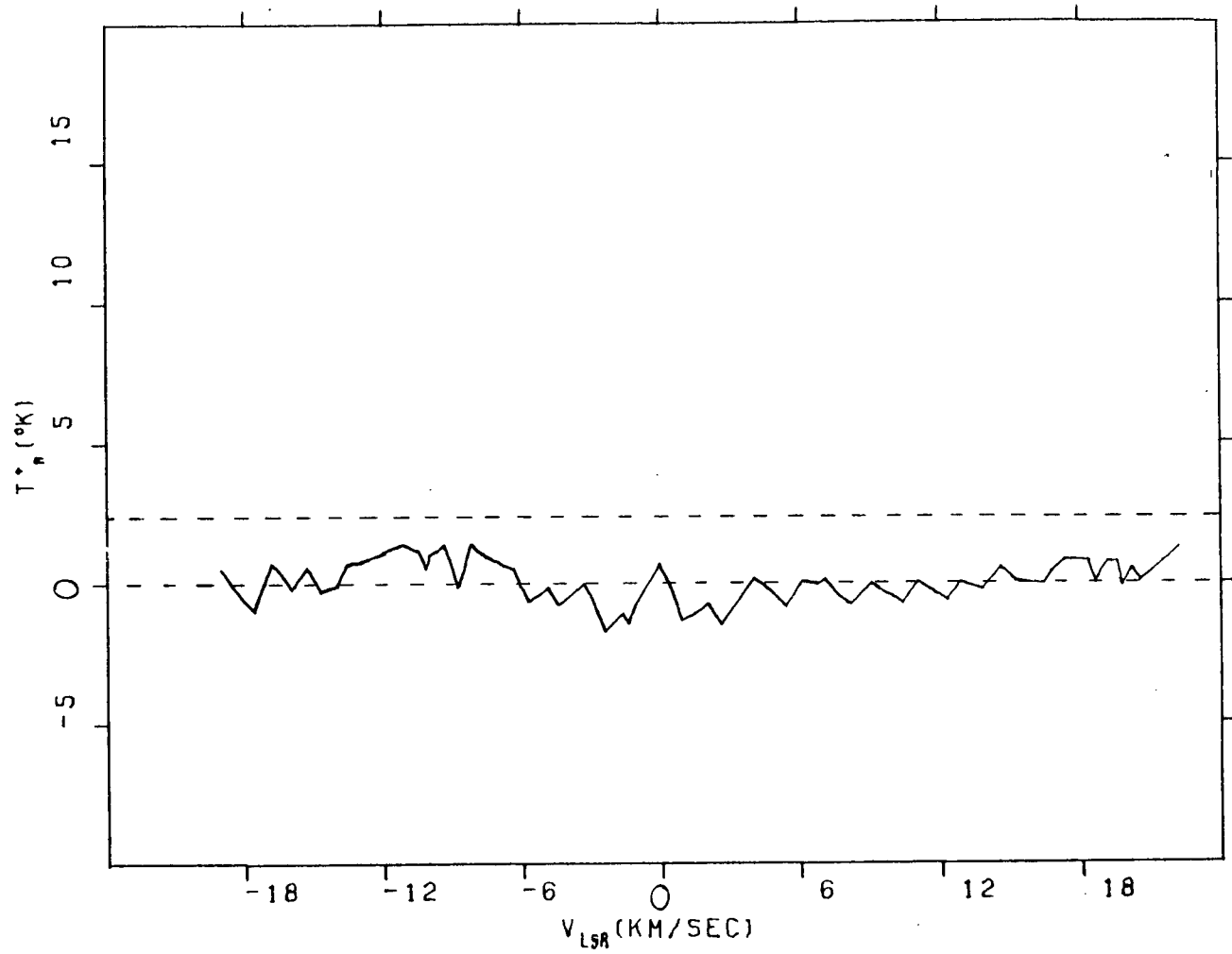
Note (5.4,-3.6) corresponds to Lk H α 101 and was used as a calibration source. Consequently, it was observed each of these days and several days before the observation program began. A total of ninety-five scans were collected giving a total integration time of 8.44 hours.

Figure 2 -Reference Position Spectrum

The figure shown is the average of twenty-eight 320 second scans for a total integration time of 2.5 hours. The peak deviation from zero signal is -1.72 kelvin. The rms noise of the spectrum is 0.75 kelvin. Also indicated is the average spectral noise for map positions (dashed line at 2.35 kelvin). The ^{12}CO signal in the reference spectrum is small even when compared with the average spectral noise. The reference position is,

$$\alpha(1950) = 04^{\text{h}}26^{\text{m}}51^{\text{s}}.7 \quad (\text{Right Ascension})$$

$$\delta(1950) = 34^{\circ}10'00''.0 \quad (\text{Declination})$$



II.4-On-Site Data Handling

A Fabri-Tek signal averager controlled by a NOVA 1200 minicomputer was used for on-site data handling. Complete details of the programs and hardware are given by Mahoney (1976). Each ON source and OFF source pair was stored on papertape. After each day of observation the four ON-OFF pairs for each map position were averaged. No weighting according to the calibration was necessary since all the observations for a single point were made on the same day using the same sky calibration. The averaged spectra were converted to an antenna temperature, T_A , using the calibration tape for that day.

Previous observations (Knapp et al. 1976, Wilson et al. 1973) had indicated the possibility of velocity structure in the far wings of the spectral line. Although this structure would have appeared at the very edge of our baselines, we found no evidence of it in our data and consequently proceeded with the analysis.

The last step of the preliminary processing was to correct the spectrum baselines by removing a second order polynomial fit to those points of the spectrum thought to have no signal (usually the first 25 and last 22 channels of the 64 channel spectrometer). This allowed us to calculate,

$$\sigma = \left\{ \frac{\left(\sum_{c=1}^{25} S_c^2 + \sum_{c=42}^{64} S_c^2 \right)}{47} \right\}^{\frac{1}{2}}$$

where c is the channel number and S_c is the signal in channel c . We adopted σ as the root mean square (rms) deviation for the spectrum. This requires the mean to be zero.

Finally, the data were not smoothed. Knapp et al. (1976) noted a self-absorption like feature in the middle of the ^{12}CO spectral line. Our results confirm that there is a prominent dip in many of the spectra, which would be lost if the data were smoothed (Figure 18).

III. DATA REDUCTION AND ANALYSIS

III.1-Calibration

This section discusses the problems encountered in finding a reliable calibration procedure for our temperature scale. Absolute calibration for millimetre wave observations is more of an art than a science. The relative temperature scale is fairly easy to determine but an absolute scale is far more elusive. We believe our calibration method has given an absolute scale with a maximum error of 20 per cent.

Spectral line observations at radio wavelengths are generally calibrated in a two step process. First, an observed signal intensity is converted to an antenna temperature, T_A . This process assumes the Rayleigh-Jeans approximation. The observed signal is compared to a calibration source with a known absolute temperature. A calibration spectrum from the synchronously detected difference output between the chopper wheel absorber at ambient temperature, T_{AMB} , and the sky was obtained. The sky temperature, T_{SKY} , was calculated by measuring the deflections from an absorber at an effective liquid nitrogen temperature of 85 K and an absorber at the ambient temperature placed in front of the feed horn. This was done at the beginning of each observing session. The end points defined by the two temperatures were checked at the end of each session. To ensure correct determination of the sky temperature we interpolated the results according to the change in the reference end points. Generally this had an insignificant effect on T_{SKY} . On nights where the atmospheric opacity changed dramatically the sky

temperature correction helped eliminate a potential error. T_{SKY} was monitored approximately every half hour and a full tipping curve measurement was carried out at the start and finish of each observing session.

The second step in the calibration process is to correct the antenna temperature for atmospheric and antenna losses to determine the true brightness temperature.

The beam efficiency, η_b , was calculated by comparing our measured T_A at various secant z 's (z is the zenith angle) to the standard values of T_A^* for OMC1(Orion A) and several other sources (Ulich and Haas 1976). We determined η_b to be about 37 per cent.

At millimetre wavelengths there are a number of difficulties in determining the atmospheric losses. This is particularly true for $J=1 \rightarrow 0$ ^{12}CO observations. One requires a knowledge of the relative sideband gains and how the attenuation in the signal sideband can be related to the average attenuation as a function of zenith angle, z , and sky temperature. There is no convenient method to determine the signal and image gains separately. The 115.271 GHz ^{12}CO $J=1 \rightarrow 0$ spectral line frequency is situated on the tail of a very strongly absorbing oxygen line and this causes the two bands to have significantly different zenith attenuations. The problem is to determine the signal zenith attenuation, τ_s , and the image attenuation, τ_i . Our tipping curves are used to measure the average attenuation, $\bar{\tau}$. If a relationship between τ_s and τ_i is known, the signal attenuation can be found.

Two summer students at U.B.C. have worked on this problem

for our telescope. From an internal report by Robert Braun (1980) on calibration procedures, we have an empirical relation for the average attenuation $\bar{\tau}$.

$$\bar{\tau} = \frac{-1}{\sec z} \ln \left[\frac{281.4 - T_{\text{SKY}}}{(1 + 0.0127 \sec^2 z) \left\{ 268.9 + 38.9 \left[1 + \left(\frac{T_{\text{AMB}} - 285}{130} \right) (1 - \sec z)^2 \right] \right\}} \right]$$

where

$$\sec z = \frac{1}{\cos z} = \frac{1}{\cos(\text{DEC}) \cos(\text{HA}) \cos(L) + \sin(\text{DEC}) \sin(L)}$$

Here DEC is the declination of the source, HA is the hour angle and L is the latitude of the telescope (49.25° North). By making plots of T_{AMB} versus $\bar{\tau}$ for varying T_{AMB} (270, 280, 290, 300) and secant z (1.0, 1.1, 1.3, 1.6, 1.8, 2.2) we solve for $\bar{\tau}$ graphically. The relation is weakly dependent on T_{AMB} and strongly dependent on secant z . From our tipping curves we obtained values for T_{AMB} at six values of secant z 's and then used the graphs to find $\bar{\tau}$. Knowing $\bar{\tau}$, we obtained τ_s from a program developed by John de Bruyn (1979). De Bruyn's program 'Atmosphere' relates τ_s and τ_i from theoretical considerations.

$$\tau_s = (1.091 \pm 0.002) \bar{\tau} + (0.123 \pm 2 \times 10^{-8})$$

and

$$\tau_i = (0.909 \pm 0.002) \bar{\tau} - (0.123 \pm 2 \times 10^{-8})$$

As we can see from these equations we have a linear relation between τ_s and $\bar{\tau}$. Unfortunately, this relationship did not always give good results. T_A^* (^{12}CO) for OMC1 varied significantly from the accepted value of 60 K. The majority of our calibration errors likely arise from some of the simplifying assumptions required by this program (eg. a parallel plane atmosphere).

Once τ_s was determined we could correct T_A for both atmospheric losses ($e^{-\tau_s \sec z}$) and the beam losses (η_B). The antenna temperature, T_A , and the true source brightness temperature, T_A^* , for a parallel plane atmosphere are related by,

$$T_A = T_A^* \eta_B \exp(-\tau_s \sec z)$$

Our data for Sharpless 222 were calibrated using two different methods. First, we calibrated all the data using the atmospheric attenuation, $\bar{\tau}$, from our tipping curve measurements. The average temperature, T_A^* (^{12}CO), for OMC1(Orion A) was 55 ± 9 K where the 9 refers to the standard

deviation of any one measurement. The average temperature, $T_A^* (^{12}\text{CO})$, for our second calibration source, Lk H α 101 (5.4,-3.6), was then found to be 12.8 K with an rms error of the mean of 0.5 K. Second, we calibrated the same raw data this time setting $T_A^* (^{12}\text{CO})$ for OMC1(Orion A) to be 60 K. This gave a new value of \mathcal{Z}_s to use to calibrate the Sharpless 222 spectra. In this case the average temperature for Lk H α 101 (5.4,-3.6) was 13.5 K with an rms error of 0.5 K. The two averaged plots of our Lk H α 101 (5.4,-3.6) calibration source are given in Figures 3 and 4.

Two map positions had $T_A^* (^{12}\text{CO})$ that appeared to be considerably lower than that of the surrounding spectra. These were Lk H α 101 (0.0,-3.6) and Lk H α 101 (7.2,-3.6). After examining the data on the two days that these were observed it was found that the temperature of the calibration source Lk H α 101 (5.4,-3.6) for Lk H α 101 (0.0,-3.6) was in fact much too low. To correct this anomaly we scaled the $T_A^* (^{12}\text{CO})$ of Lk H α 101 (5.4,-3.6) for this day up to the average $T_A^* (^{12}\text{CO})$, namely 13.5 K. The point Lk H α 101 (0.0,-3.6) was corrected using the new \mathcal{Z}_s from the scaled calibration source. The spectrum at Lk H α 101 (7.2,-3.6) appears to have a bad channel located in the profile. This results from a random D.C. offset that periodically appears in one or two channels of the spectrometer. It was decided that there was no evidence to alter this spectrum and that it should have been repeated. Unfortunately, the telescope experienced technical difficulties throughout the remainder of this project that prevented any more spectra being taken.

During four sessions our tipping curves indicated a two component atmosphere that was dependent on zenith angle. Each component had a different atmospheric attenuation, $\bar{\tau}$, and as a result the calibration errors for these days were higher. We estimate that the error does not exceed 20 per cent. In conclusion, we believe the bulk of our data has a maximum calibration error of 20 per cent. Repeatability checks at several grid positions confirmed this estimate. Calibration is a very tricky procedure that requires consistent checks and precautions to maintain reliable results. We feel that all the precautions helped simplify and reduce our calibration errors. For millimetre wave radio astronomy careful calibration procedure is essential to good data.

Figure 3 -Lk H α 101 (5.4,-3.6)-Tipping Curve Calibration

This spectrum is the average of ninety-five 320 second scans. The total integration time is 8.44 hours. The location coincides with the exciting star Lk H α 101,

$$\alpha(1950) = 04^{\text{h}} 26^{\text{m}} 51.7^{\text{s}} \quad (\text{Right Ascension})$$

$$\delta(1950) = 35^{\circ} 10' 00.0'' \quad (\text{Declination})$$

The temperature was calibrated using the daily tipping curve measurements. The velocity is the average for all ninety-five scans (rms error of the mean is 0.07 km s^{-1}).

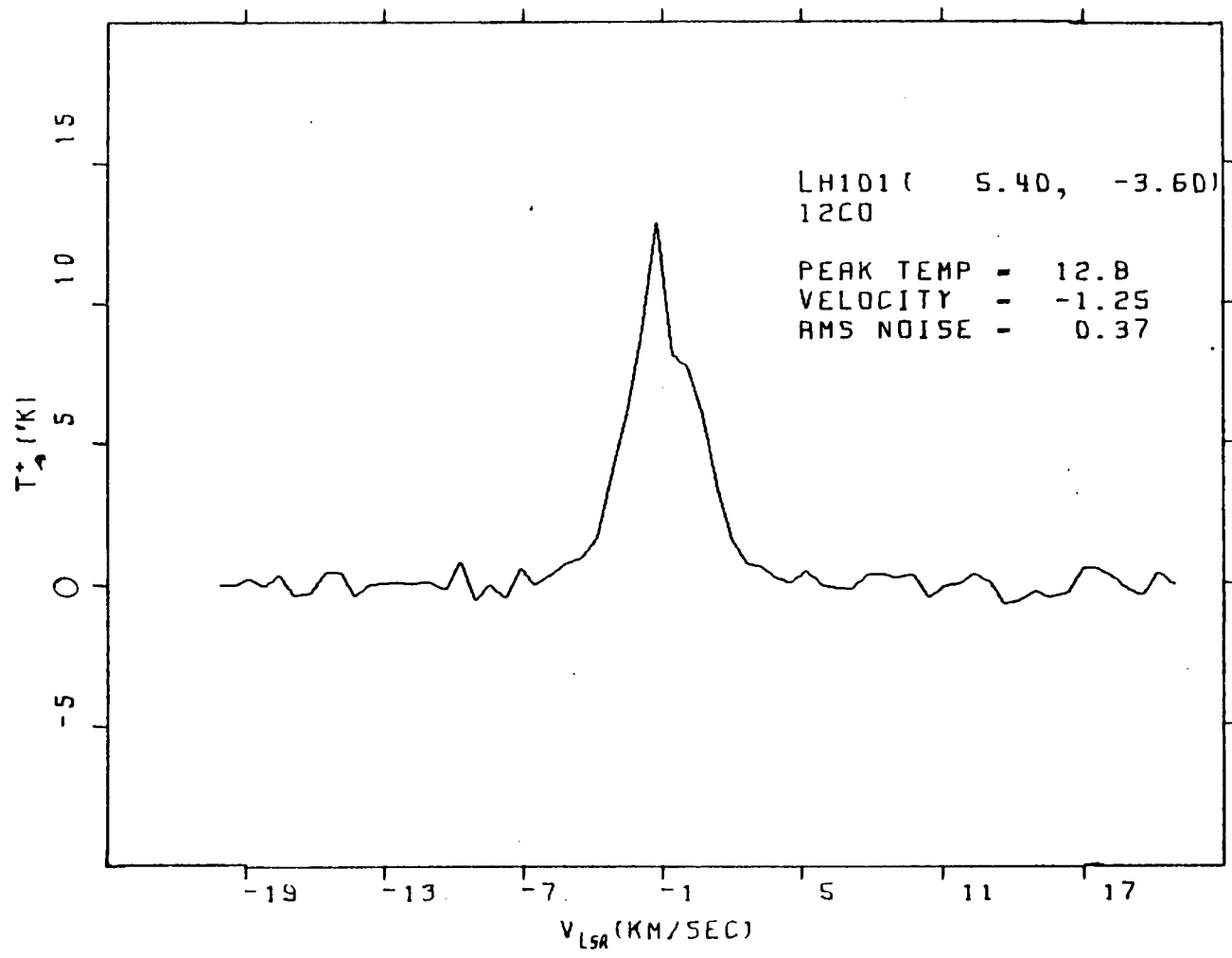


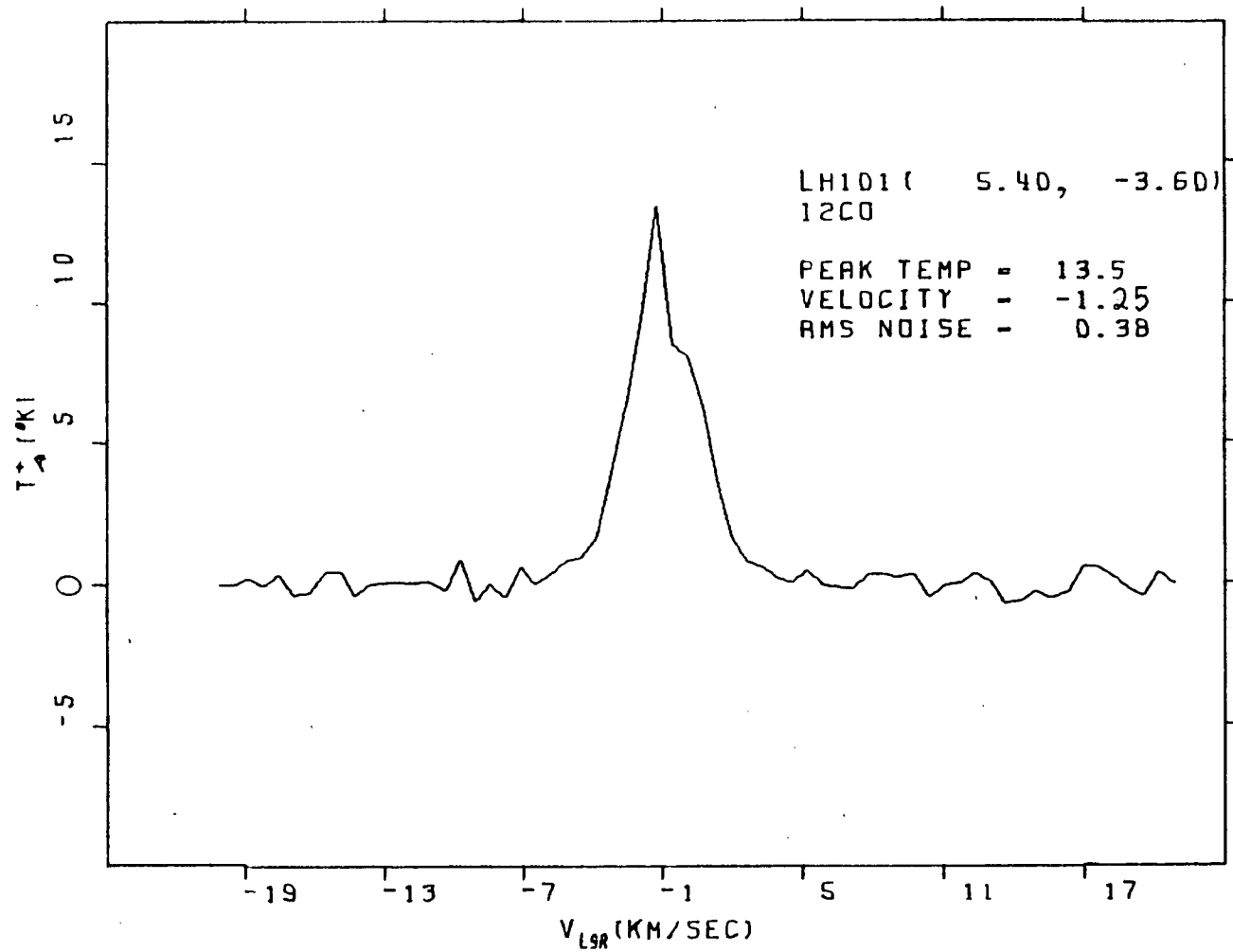
Figure 4 -Lk H α 101 (5.4,-3.6)-OMC1(Orion A) Calibration

This spectrum is the average of ninety-five 320 second scans. The total integration time is 8.44 hours. The location coincides with the exciting star Lk H α 101,

$$\alpha(1950) = 04^{\text{h}}26^{\text{m}}51^{\text{s}}.7 \quad (\text{Right Ascension})$$

$$\delta(1950) = 35^{\circ}10'00''.0 \quad (\text{Declination})$$

The temperature was calibrated using OMC1(Orion A) as the calibration source. T_{A}^* (^{12}CO) for OMC1(Orion A) was taken to be 60 K. The velocity is the average for all ninety-five scans (rms error of the mean is 0.07 km s^{-1}).



III.2-Representation Of Lk H α 101 Through Global Plots

We present Sharpless 222 results in two different complementary formats. The first is contour plots of declination (DEC) versus right ascension (RA) for a fixed line velocity. The second is that of global plots as shown in Figures 5 and 6. We did not use colour contours since the U.B.C. computing centre does not have a full colour graphics package. The centre does have colour intensity contours. Szabo (1980) found these were unsuitable since the human eye can not distinguish the intensities properly.

Global plots have the distinct advantage of showing the entire region and general features quite well; however it is difficult to see how smaller features at different positions correlate. The contour plots show the smaller features and their correlations with position very well. In this way we gain maximum information in relatively simple formats.

Figure 5 is the global plot of the spectral positions calibrated using the atmosphere transparency determined from the antenna tipping measurements. One correction, Lk H α 101 (0.0,-3.6), is based on the Lk H α 101 (5.4,-3.6) calibration source. Figure 6 is the global plot of the spectral positions calibrated using OMC1(Orion A) as a calibration source. The same correction for position (0.0,-3.6) has been made. The calibrations made using OMC1 as the calibration source were found to be slightly better than those from the tipping curves. For this reason we decided to use this data for the remaining analysis. Full details are given in chapter IV.

Figure 5 -Global Plot (Tipping Curve Calibration)

All eighty-nine spectral positions are indicated. The temperature scale is 95.00 K in^{-1} and the L.S.R. velocity range is -23 to 24 km s^{-1} . There is one correction based on the Lk H α 101 (5.4,-3.6) calibration source. This is position Lk H α 101 (0.0,-3.6). The remaining spectral positions were calibrated using the daily tipping curve measurements. The central position is,

$$\alpha(1950) = 04^{\text{h}} 26^{\text{m}} 34^{\text{s}}.0 \quad (\text{Right Ascension})$$

$$\delta(1950) = 35^{\circ} 13' 00''.0 \quad (\text{Declination})$$

LH101

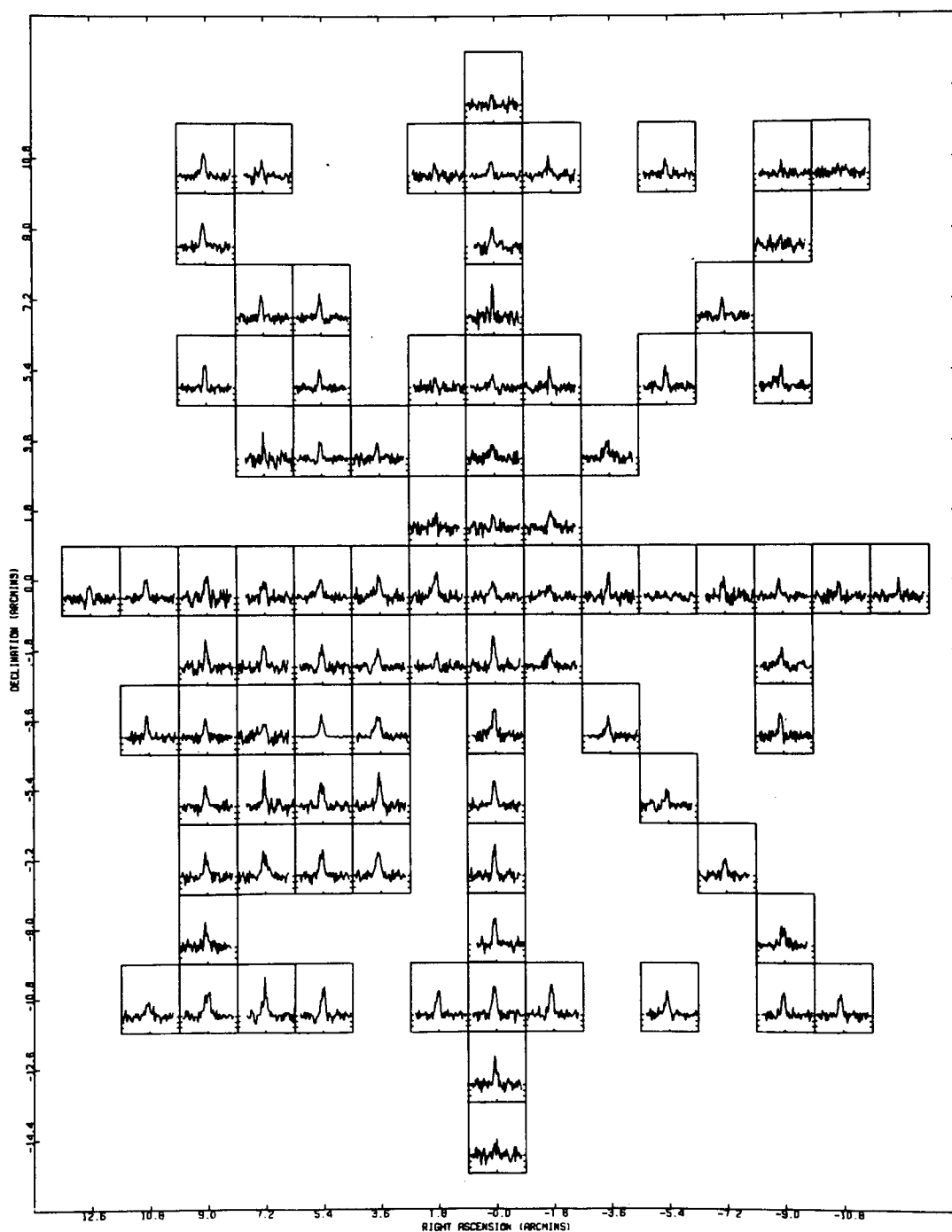


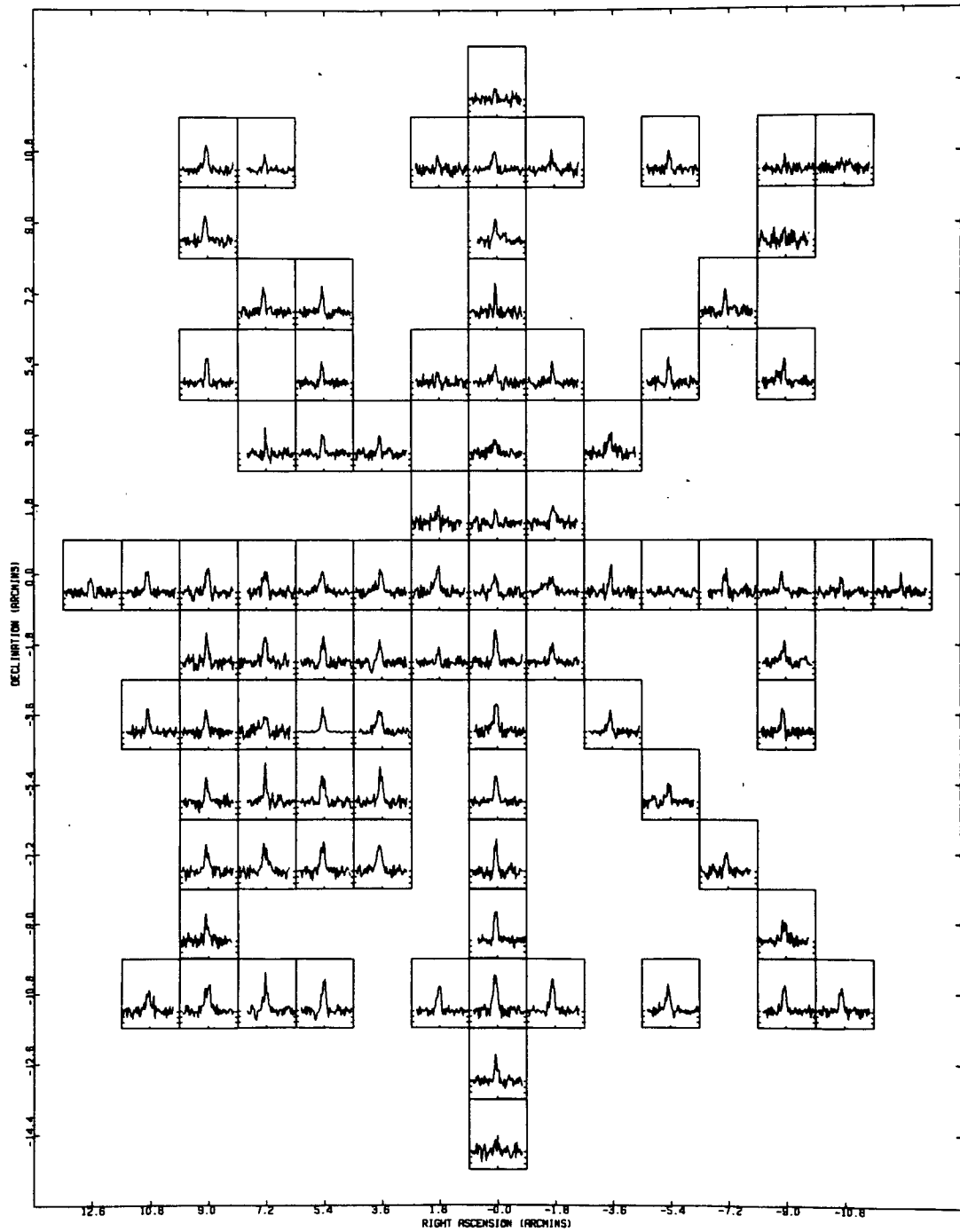
Figure 6 -Global Plot (OMC1(Orion A) Calibration)

All eighty-nine spectral positions are indicated. The temperature scale is 89.80 K in^{-1} and the L.S.R. velocity range is -23 to 24 km s^{-1} . There is one correction based on the Lk H α 101 (5.4,-3.6) calibration source. This is position Lk H α 101 (0.0,-3.6). The remaining spectral positions were calibrated using OMC1(Orion A) as the calibration source. T_A^* (^{12}CO) for OMC1 was taken to be 60 kelvin. The central position is,

$$\alpha(1950) = 04^{\text{h}}26^{\text{m}}34.5^{\text{s}} \text{ (Right Ascension)}$$

$$\delta(1950) = 35^{\circ}13'00.0'' \text{ (Declination)}$$

LH101



III.3-¹²CO Radiation Temperatures

The velocity resolution available is determined by the bandpass of the spectrometer. Our spectrometer has filter widths of 250 KHz which corresponds to a velocity resolution of 0.65 km s⁻¹ at the J=1→0 transition of ¹²CO. The frequency counter used to check the crystal frequency is accurate only to about 125 KHz. The main reason for this is the drift of the crystal frequency itself. To minimize this problem the counter was continually monitored such that the resulting error never exceeded 125 KHz. Another error that has subsequently been corrected lies in our Local Standard of Rest (L.S.R.) program. The velocity resulting from the earth's motion is subtracted from the observed velocity information. Our program, described in Mahoney (1976), did not take partial Julian days into account when calculating the L.S.R. Subsequent analysis has shown that the maximum error incurred is less than one half a spectrometer channel. Summing over the possible sources of velocity errors we see that the total error is at the limit of our resolution. This is 0.65 km s⁻¹.

In determining the central velocity of the spectral profile for Sharpless 222 we used two independent methods. The difference between the L.S.R. velocities for Sharpless 222 and OMC1(Orion A) at the beginning of our observing program was such that we could just fit both spectra into the spectrometer bandpass using the same crystal frequency. This was done by switching between two local oscillators spaced 8.0 MHz. apart. Since we know the frequency difference between the two

oscillators to a high degree of accuracy we could calculate the resulting Sharpless 222 profile velocity. We assumed a velocity for the ^{12}CO profile in OMC1(Orion A) of 9.0 km s^{-1} . This gave a velocity for Sharpless 222 of -1.25 km s^{-1} for the (5.4,-3.6) position. The second method used a crystal frequency designed to place a line having $V_{\text{LSR}} = 0 \text{ km s}^{-1}$ into channel 33. The central velocity for Lk H α 101 (5.4,-3.6) was found to be -1.25 km s^{-1} as before.

The spectral profile for OMC1(Orion A) is about 5 km s^{-1} wide. Adoption of a central velocity of 9.0 km s^{-1} on such a wide profile would normally have a large error associated with the velocity since the centre of a wide line is not as precisely defined as that of a narrow line. Since OMC1(Orion A) was used as the primary calibration source we have 36 profiles that give an average central velocity of 8.92 km s^{-1} with an rms error of 0.04 km s^{-1} . The standard deviation for any one measurement was 0.25 km s^{-1} . This result agrees very well with the assumed value of 9.0 km s^{-1} . It should also be noted that two very different procedures gave the same central velocity for Sharpless 222.

We have a total of 95 scans for the calibration source Lk H α 101 (5.4,-3.6). The average velocity determined from these scans is -1.25 km s^{-1} with an rms error in the mean of 0.07 km s^{-1} . The standard deviation of any single measurement is 0.33 km s^{-1} which is less by a factor of two than our velocity resolution. Knapp et al. (1976) obtained a central profile velocity for Lk H α 101 (5.4,-3.6) of approximately $-1 \pm 1 \text{ km s}^{-1}$. This is in excellent agreement with our results.

From both sets of data calibrated using the two methods we

obtained T_A^* (^{12}CO) contour maps for fixed L.S.R. velocities. Comparison of these contours indicates that they are very nearly identical. Figure 7 shows the T_A^* (^{12}CO) contour map integrated over all L.S.R. velocities.

To check the reality of the contour features we varied the fixed velocity by small increments. We found the changes in the features were negligible, certainly far less than our velocity resolution. The spatial resolution of most of the features on the T_A^* (^{12}CO) contours is only marginal. Unresolved features could be caused by incorrect calibration for one grid position and consequently the reality of these features may be suspect. Due to this fact, we cannot say very much about the structure or spatial details of Sharpless 222.

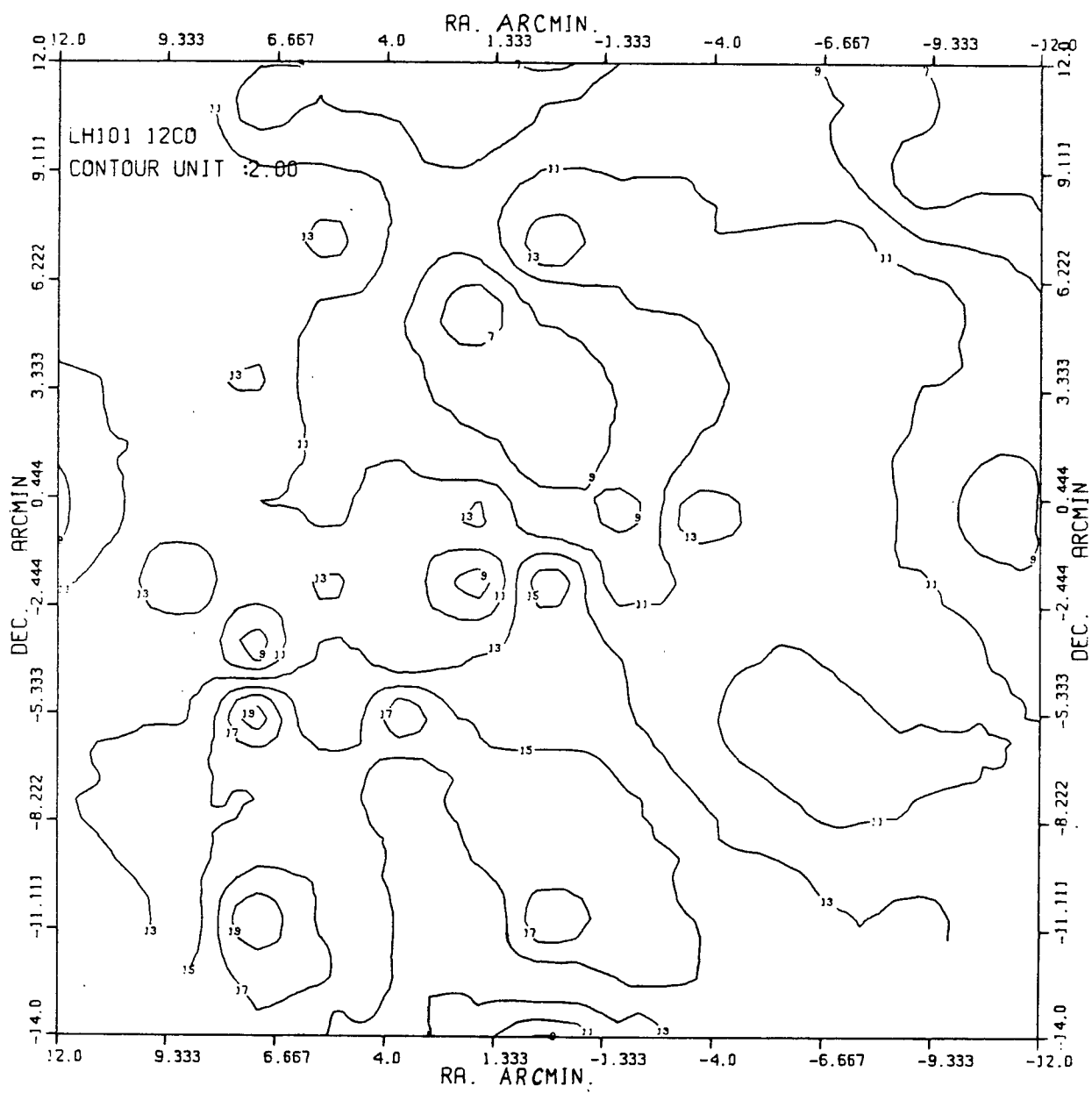
Full details of the structure and size of our cloud are given in chapter four.

Figure 7 -Integrated ^{12}CO Contours

The T_A^* (^{12}CO) is integrated over all velocities to give Figure 7. The declination (DEC) versus right ascension (RA) plot shows the five hottest spots to be located at (7.2,-10.8), (0.0,-10.8), (7.2,-5.4), (3.6,-5.4), and (0.0,-1.8). The units for both axis are arcminutes. The centre (0.0,0.0) is,

$$\alpha(1950) = 04^{\text{h}}26^{\text{m}}34.0^{\text{s}} \quad (\text{Right Ascension})$$

$$\delta(1950) = 35^{\circ}13'00.0'' \quad (\text{Declination})$$



III.4-Generating Model For ^{13}CO

Although ^{13}CO observations were not made, approximate data can be generated. Two simplifying assumptions have to be made. First, we need to know the ratio of the ^{12}CO to ^{13}CO emission temperatures. Secondly, we require the profile half widths for ^{13}CO . It must be emphasized that these data are only a rough approximation and are not a good substitute for real observations. As a result, the generated ^{13}CO data are used only to reinforce the conclusions apparent from the ^{12}CO observations.

In order to calculate the opacity of ^{13}CO , $\tau(^{13}\text{CO})$, we require values for the ^{13}CO radiation temperature, $T_A^*(^{13}\text{CO})$, for each of the spectral positions. Recent data obtained by Sewall (1980) have been very beneficial in this regard. He found that the ^{13}CO profiles mimicked the ^{12}CO profiles in shape and that the ^{13}CO radiation temperatures were approximately five times lower than those for the ^{12}CO . Figure 8 is a plot of $T_A^*(^{13}\text{CO})$ versus the ratio of $T_A^*(^{12}\text{CO})$ to $T_A^*(^{13}\text{CO})$ for the three Sharpless regions studied by Sewall (1980). The result is a power law relation that can be used to give an estimate for $T_A^*(^{13}\text{CO})$ from our $T_A^*(^{12}\text{CO})$. Knapp et al. (1976) observed both ^{12}CO and ^{13}CO in Sharpless 222 at two positions. The average ratio of their radiation temperatures is five. This indicates that the temperature ratio for Sharpless 222 behaves much like the other Sharpless regions studied by Sewall (1980). Therefore, we can estimate the magnitude and variation of this ratio for Sharpless 222 using the results of other Sharpless regions from

Sewall (1980). The estimates are summarized in Table II. The ratio of $T_A^* (^{12}\text{CO})$ to $T_A^* (^{13}\text{CO})$ was linearly interpolated for values within a given range of $T_A^* (^{12}\text{CO})$. Some subjective assessments of the interpolation were made according to the extent of the emission regions. For large emission areas the ratio was usually decreased by 0.1 to 0.2 and for very small areas of low emission the ratio was increased by the same amounts. The estimates for the ^{13}CO temperature are rough approximations. Extending this method to individual sources such as Sharpless 222 should only be done as a last resort. Data from ^{13}CO observations are always preferable.

We believe this method has enabled us to estimate $T_A^* (^{13}\text{CO})$ to within 25 per cent. The results of the peak $T_A^* (^{13}\text{CO})$ for -1.25 km s^{-1} are illustrated in Figure 9. This contour plot clearly shows the hot spots embedded in a cooler background of ^{13}CO emission. These results will be discussed in greater detail in the next chapter.

Using derived values for $T_A^* (^{13}\text{CO})$, we determined $\tau (^{13}\text{CO})$ from the standard formula,

$$\tau (^{13}\text{CO}) = -\text{Ln} \left(1 - \frac{T_A^* (^{13}\text{CO})}{T_A^* (^{12}\text{CO})} \right)$$

This equation assumes that the ^{12}CO and ^{13}CO excitation temperatures are equal. One expects this to be approximately true but as we will see this may not be valid whenever there is

a distinct dip in the spectral profile. The energies of the $J=1$ levels of the two isotope species are very nearly equal. The excitation temperature for ^{12}CO is probably larger and closer to the local gas kinetic temperature than that of the optically thin ^{13}CO . This is due to the fact that there is significant radiation trapping occurring with the optically thick ^{12}CO line. This means that the ^{13}CO opacities calculated with the formula above are actually lower limits of the real value.

The results $T_A^* (^{13}\text{CO})$ and $\tau(^{13}\text{CO})$ are summarized in Table VI following this chapter.

| $T_A^* (^{12}\text{CO})$ (kelvin) | Ratio $T_A^* (^{12}\text{CO})/T_A^* (^{13}\text{CO})$ |
|--------------------------------------|--|
| >20 | <3.5 |
| 16→20 | 4.0→3.5 |
| 10→16 | 5.0→4.0 |
| <10 | 7.5→5.0 |

Table II - $T_A^* (^{13}\text{CO})$ Generating Model

Table II details estimates of the ratio $T_A^* (^{12}\text{CO})$ to $T_A^* (^{13}\text{CO})$ for different values of $T_A^* (^{12}\text{CO})$. These result from an analysis of data on Sharpless regions compiled by Sewall (1980).

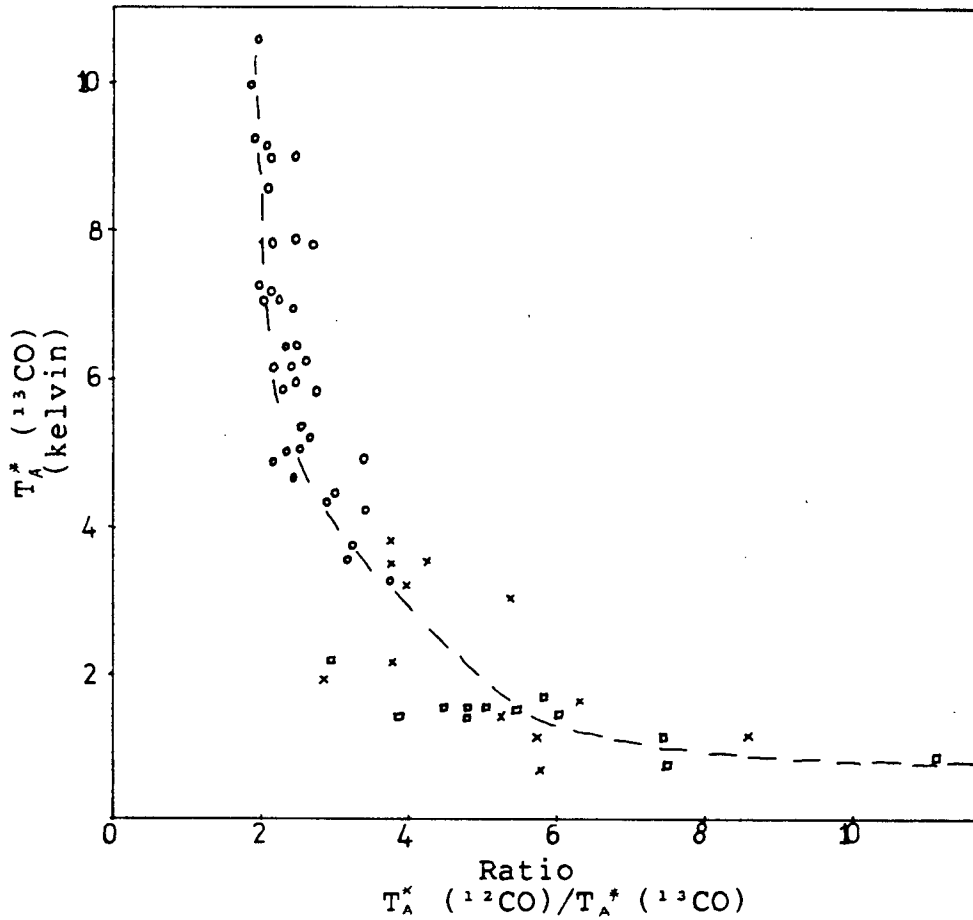


Figure 8 - $T_A^* (^{13}\text{CO})$ Vs. $T_A^* (^{12}\text{CO})/T_A^* (^{13}\text{CO})$ Ratios

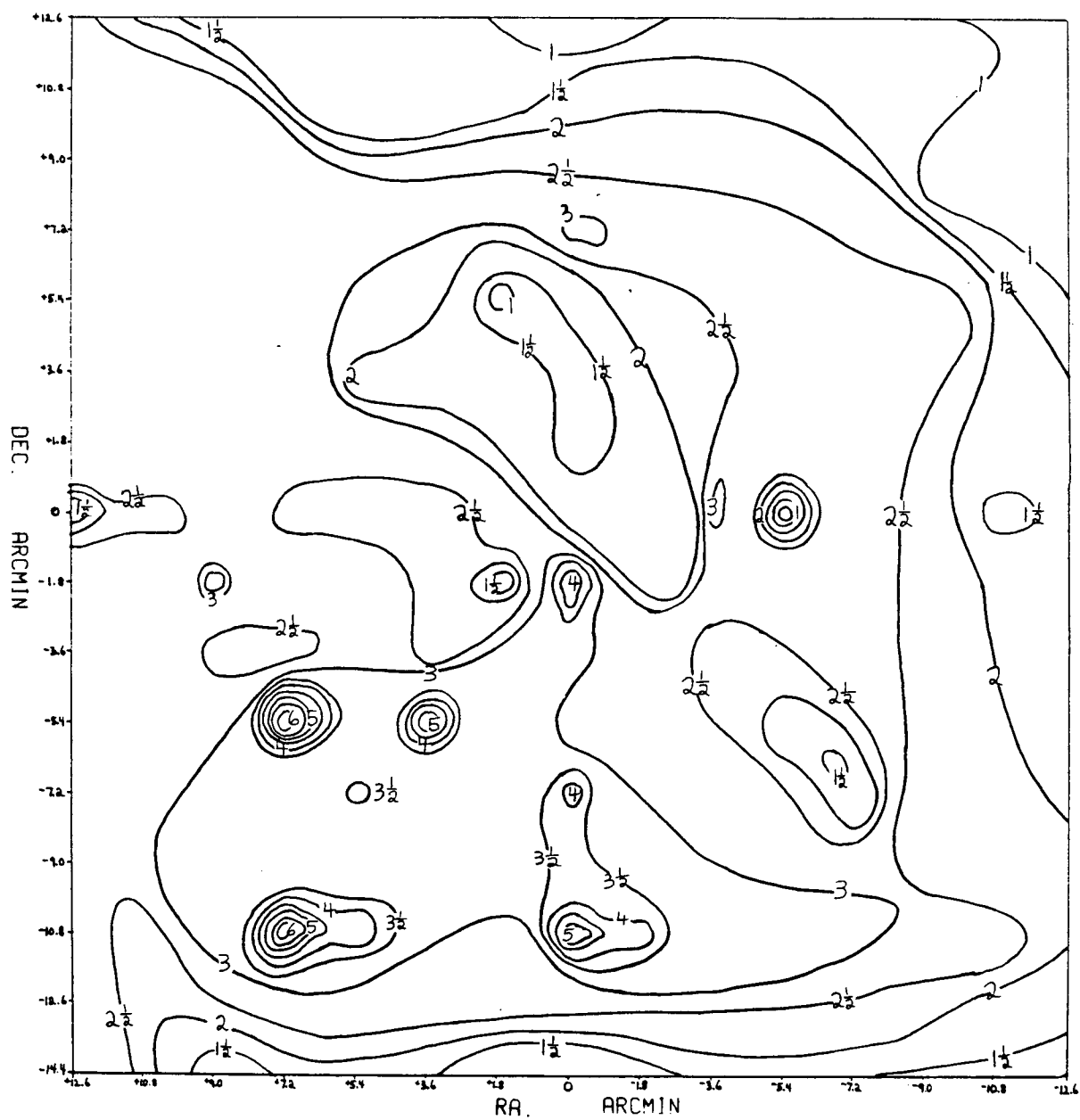
The ratios were obtained from data of Sewall (1980). Circles are Sharpless 152 data, crosses are Sharpless 206 data, and boxes are Sharpless 148 data. This result was used to generate the $T_A^* (^{13}\text{CO})$ (see Table II- $T_A^* (^{13}\text{CO})$ Generating Model).

Figure 9 -Generated T_A^* (^{13}CO) Contours

The T_A^* (^{13}CO) contours are generated from ^{12}CO observations. The contour units are 0.5 K steps. The declination (DEC) verses right ascension (RA) plot shows the same five CO hot spots present in Figure 7 (T_A^* (^{12}CO) Contours). The units for both axis are arcminutes. The centre (0.0,0.0) is,

$$\alpha(1950) = 04^{\text{h}}26^{\text{m}}34^{\text{s}}.0 \quad (\text{Right Ascension})$$

$$\delta(1950) = 35^{\circ}13'00''.0 \quad (\text{Declination})$$



III.5-Generated ^{13}CO Column Densities

To obtain an estimate for the ^{13}CO column density, $N_{\text{COL}}(^{13}\text{CO})$, we require values for the half power line widths of the expected ^{13}CO profiles. Since ^{13}CO was not observed in our survey we decided to study pairs of ^{12}CO and the corresponding ^{13}CO profiles for other Sharpless regions to determine if there exists a relationship between half power line widths for ^{12}CO and ^{13}CO profiles. The results are given in Table III. S152 and S148 refer to two of the three Sharpless regions studied by Sewall (1980). S222 and S239 are taken from Knapp *et al.* (1976). The ratio , $\Delta V(^{12}\text{CO})$ to $\Delta V(^{13}\text{CO})$, adopted was 1.52 with a standard deviation of 0.10 in any one measurement or an rms error of 0.04 in the average.

We found $\Delta V(^{12}\text{CO})$ visually from our spectral profiles for each of the 89 positions. To check the accuracy of this method we assumed the best gaussian fit to six of our profiles chosen at random. The resulting $\Delta V(^{12}\text{CO})$ from the gaussian profile was found to be 20 ± 2 per cent larger than the visually measured half widths. We decided to measure $\Delta V(^{12}\text{CO})$ visually since a gaussian profile was obviously not a good fit for our data. The gaussians have wings that extend too far with a net result of the gaussians becoming too wide if the peak temperature of the observed profile is to be maintained. The alternative is to reduce the width of the gaussian. Unfortunately, this also reduces the peak temperature which was deemed unacceptable. A summary of the two methods is given in Table IV.

Once $\Delta V(^{12}\text{CO})$ was found visually, $\Delta V(^{13}\text{CO})$ was determined

by dividing each $\Delta V(^{12}\text{CO})$ by the ratio of $\Delta V(^{12}\text{CO})$ to $\Delta V(^{13}\text{CO})$ (i.e. 1.52). The column density for ^{13}CO , $N_{\text{COL}}(^{13}\text{CO})$, was calculated using a relation derived by Morris as quoted in Sewall (1980).

$$N_{\text{COL}}(^{13}\text{CO}) = \frac{2.6 \tau(^{13}\text{CO}) \Delta V(^{13}\text{CO}) [T_{\text{ex}}(^{13}\text{CO}) + 0.9]}{1 - \exp\left(\frac{-5.29}{T_{\text{ex}}(^{13}\text{CO})}\right)} \times 10^{14} \text{ cm}^{-2}$$

where $T_{\text{ex}}(^{13}\text{CO})$ is calculated from,

$$T_{\text{ex}}(^{13}\text{CO}) = T_{\text{ex}}(^{12}\text{CO}) = 5.53 \ln \left\{ 1 + \frac{5.53}{T_A^*(^{12}\text{CO}) + 0.83} \right\}$$

Morris notes that the assumption $T_{\text{ex}}(^{13}\text{CO}) = T_{\text{ex}}(^{12}\text{CO})$ must be used once more in calculating the column density for ^{13}CO . This time the error incurred is in the opposite sense as that introduced in the ^{13}CO opacity calculation. Since $T_{\text{ex}}(^{13}\text{CO})$ and $\tau(^{13}\text{CO})$ are multiplied together in the column density expression the error is substantially reduced. As long as $T_{\text{ex}}(^{12}\text{CO}) \cong T_{\text{ex}}(^{13}\text{CO})$, which seems to be a reasonable assumption for Sharpless regions, then the errors should very nearly cancel; otherwise the $N_{\text{COL}}(^{13}\text{CO})$ estimate is a lower limit.

Figure 10 represents the column densities. We believe there are three well resolved clouds: cloud #1, #2, and #3. They are located at Lk H α 101 (7.2, -10.8), Lk H α 101 (0.0, -10.8), and Lk H α 101 (7.2, -5.4) respectively. Another two possible fragmentations were treated in this project. Extreme care should be exercised since they are on the very limit of our spatial

resolution. Examination of the ^{12}CO profiles indicates these clouds, #4 and #5, are probably real. They are located at Lk H α 101 (3.6,-5.4) and Lk H α 101 (0.0,-1.8).

It cannot be emphasized enough that the generated ^{13}CO data is only an approximation and should not be relied upon too heavily. The ^{12}CO observations form the basis of our observing program and as such are the very core of our conclusions. All of our fragmentations appear real on the ^{12}CO global plots.

| Source | Position | $\Delta V(^{12}\text{CO})$ | $\Delta V(^{13}\text{CO})$ | Ratio |
|---------------------------------|----------|----------------------------|----------------------------|-------|
| S152 | W1S1 | 5.4 | 3.7 | 1.47 |
| | E1S1 | 5.0 | 3.2 | 1.55 |
| S148 | E0S1 | 3.9 | 2.8 | 1.40 |
| S222 | E0N0 | 4.0 | 2.7 | 1.49 |
| | E0N1 | 3.6 | 2.1 | 1.70 |
| S239 | E0N0 | 2.5 | 1.4 | 1.59 |
| | E2N0 | 1.6 | 1.0 | 1.46 |
| average = 1.52 ± 0.04 (rms) | | | | |

Table III -Profile Half Width Ratios

Our ^{13}CO profile half widths were calculated using the observed ^{12}CO profile half widths. Data for four Sharpless regions Knapp et al. 1976, Sewall 1980) show the ratio of $\Delta V(^{12}\text{CO})$ to $\Delta V(^{13}\text{CO})$ is remarkably constant. The $\Delta V(^{13}\text{CO})$ in our survey was determined by dividing the measured $\Delta V(^{12}\text{CO})$ by the average ratio 1.52.

| Parameter | Method | | Deviation between the two methods. |
|----------------------------|--|---|------------------------------------|
| | Visual | Gaussian | |
| Velocity | Directly from spectral plot program, same as gaussian. | $\bar{V} = \frac{\sum_{i=1}^n T_{Ai}^* V_i}{\sum_{i=1}^n T_{Ai}^*}$ | <1% |
| Standard deviation | Directly from spectral plot program, same as gaussian. | $\sigma^2 = \sum_{i=1}^n \frac{(V_i - \bar{V})^2}{n-1}$ | <1% |
| $\Delta V(^{12}\text{CO})$ | Visual est. | $\Delta V = 2\sqrt{2 \log_e 2} \sigma$ | $20 \pm 2\%$ high for gaussian |

Table IV -Velocity Calculations

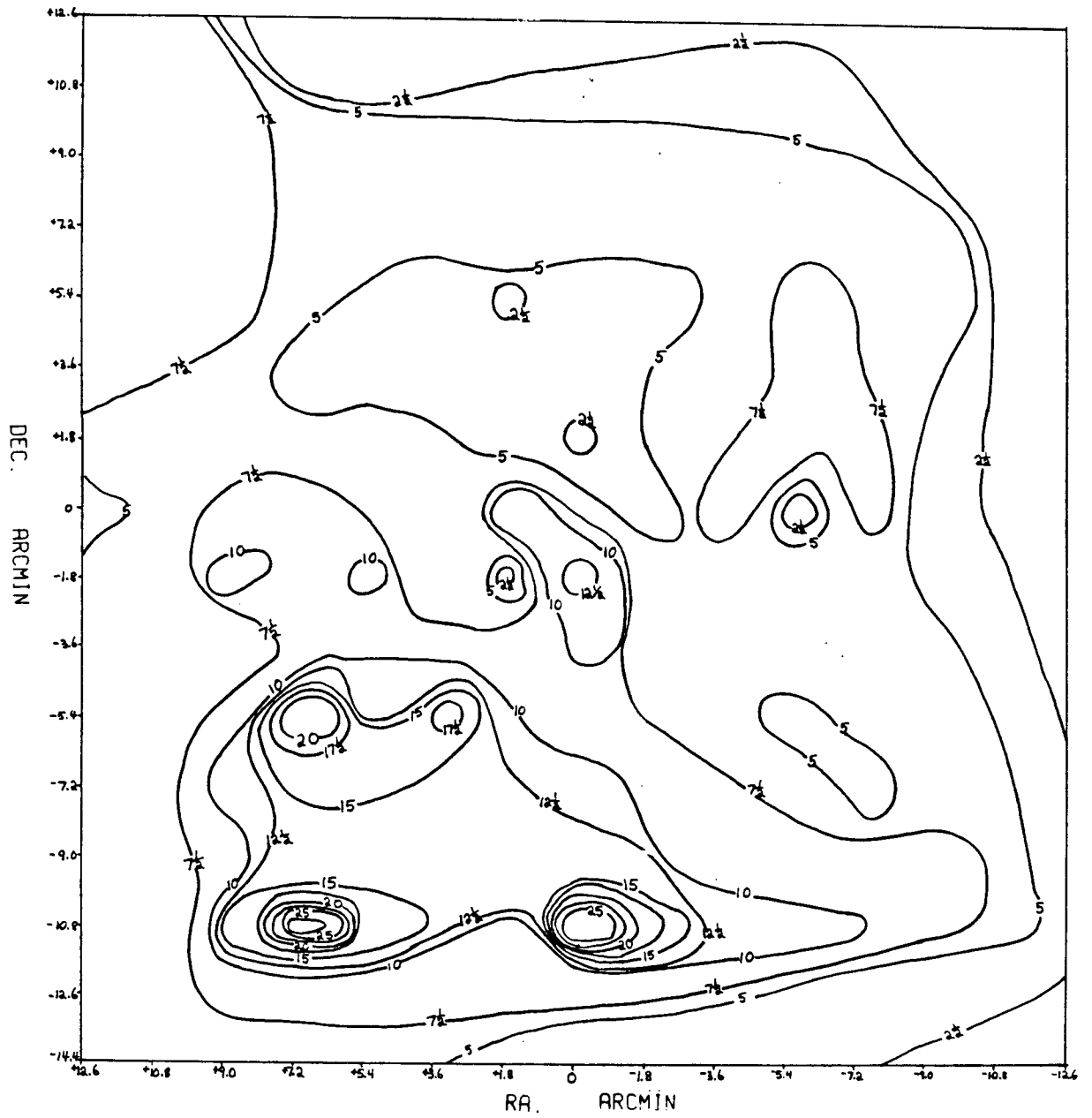
This data summarizes the two approaches used to determine the velocity of each profile, the standard deviation of each profile, and the profile half widths. Differences between visual inspection and gaussian fitting resulted only for values obtained for profile half widths. The value from the gaussian fit is high by about twenty per cent. This is due to the sharpness of the observed profile shapes. Gaussian curves are much flatter than the observed profiles and as a result are poor representations of the observed data.

Figure 10 Generated $N_{\text{COL}}(^{13}\text{CO})$ Contours

The $N_{\text{COL}}(^{13}\text{CO})$ contours are generated from ^{12}CO observations. The contour units are $1 \times 10^{15} \text{ cm}^{-2}$. The declination (DEC) versus right ascension (RA) plot shows the same five CO hot spots present in Figure 7 ($T_{\text{A}}^*(^{12}\text{CO})$ Contours). The units for both axis are arcminutes. To determine $N_{\text{COL}}(^{13}\text{CO})$, the ratio $\Delta V(^{12}\text{CO})$ to $\Delta V(^{13}\text{CO})$ was found to be 1.52 ± 0.04 (see Table III-Profile Half Width Ratios). The centre (0.0,0.0) is,

$$\alpha(1950) = 04^{\text{h}}26^{\text{m}}34.5^{\text{s}} \quad (\text{Right Ascension})$$

$$\delta(1950) = 35^{\circ}13'00.0'' \quad (\text{Declination})$$



III.6-Star Counting Theory, Data And Results

The basic procedure used here for star counting is that described by Dickman (1978). Enlarged prints and the originals of the red and blue Palomar prints were used for the star counts. The data from both sets of prints agreed. A transparent grid of 'reseau' squares was placed on the print. The size of the grid used was 1.8 arcminutes. This is the spacing between half power points of our telescope beam and also the spacing used in our map. All counts were made with the aid of a low power microscope.

All stars in a given square were counted without regard to their magnitudes. This was adopted because the small grid size would have introduced very large statistical uncertainties due to the small number of stars in each square with a particular magnitude. The statistical error expected with a count of 'n' stars in any square is \sqrt{n} (Bok 1937). Star counting was performed twice for each of the blue and red prints.

Star counts for the reference fields were made in each of the four corners outside the region of obscuration. Both Palomar prints were used. The presence of any obscuration in the reference regions leads to a systematic underestimate of the extinction in the cloud. As a result, considerable care is needed in selecting the reference field to minimize the apparent obscuration. Star counting in each of the four corners was repeated for both colours. The limiting magnitude determined was 18.83 ± 0.10 for the red print and 18.18 ± 0.25 for the blue print.

The number of stars counted in each square was averaged with adjacent values in order to obtain a more uniform distribution consistent with the resolution of our CO contours. The weighted average of the star counts used had very little effect on squares with one or more stars. In regions where no stars were counted a result was obtained from the smoothing of the immediate neighbours. This is probably more accurate than just assigning one star over each region without any stars, as was done by Dickman (1978). The weighting function used is as follows:

$$\text{Weighted Star Count} = \frac{2}{3} \left(\begin{array}{c} \text{star count in} \\ \text{the square} \\ \text{of interest} \end{array} \right) + \frac{1}{3} \left(\begin{array}{c} \text{Averaged star count} \\ \text{in the 9 squares} \\ \text{centred on the square} \\ \text{of interest} \end{array} \right)$$

The weighted star counts for each grid element are then used to determine an effective extinction. This was done utilizing tables compiled by van Rhijn (1929). These tables contain smoothed values of the logarithm of the number of stars per square degree, brighter than an apparent photographic magnitude, m , and given in ten degree steps of galactic longitude. The table actually used for this work is contained in Allen's "Astrophysical Quantities".

Van Rhijn's tables have long been in question. Considerable corrections had to be used to reconcile the different magnitude systems in the star catalogues used in his compilations. Unfortunately, these tables remain the only source of

information for general star counts.

Van Rhijn's tables give $\log N$ as a function of the old photographic magnitude. Here N refers to the number of stars counted per square degree at a specific galactic longitude. The old photographic magnitude is very nearly the same as the modern blue magnitudes. In reducing the blue counts from the Palomar prints we simply used the table adjusted for a galactic latitude of -9.0 degrees. The interpolated results from Allen are given in Table V.

If one counts the number of stars per square degree in the reference region, one may assign a limiting magnitude, $m(\text{ref})$, to these counts. If at some point inside the cloud one repeats the same procedure then the corresponding magnitude, $m(\text{pt})$, should be less than $m(\text{ref})$. This means fewer stars are seen through the obscuring cloud. The extinction at that point is then, $A(\text{pt}) = m(\text{ref}) - m(\text{pt})$ magnitudes in the blue.

Since van Rhijn's tables are only valid for blue magnitudes we have to find a similar approach for the red print. An important property of the van Rhijn tabulations is their near linearity close to the galactic plane. Therefore, we can write $\log N(m_b) = a_b + b_b m_b$. Dickman (1978) considers a series solution for the corresponding relationship for red magnitudes (i.e. $\log N(m_r) = a_r + b_r m_r + c_r m_r^2 + \dots$). To the first order he finds that $c_r \cong 0$ and $b_r \cong b_b$. Therefore, one can treat the red magnitudes in exactly the same manner as the blue magnitudes. For the blue magnitudes we have

$$A_b = \frac{1}{b_b} \log \frac{N_b(\text{ref})}{N_b(\text{pt})}$$

where $b_b \cong 0.35$ from van Rhijn. For the red magnitudes we have

$$A_R = \frac{1}{b_b} \log \frac{N_R(\text{ref})}{N_R(\text{pt})}$$

since $b_R \cong b_b \cong 0.35$.

The final step is the reduction of the two colour magnitudes to some standard colour magnitude. It is conventional to take $V = 5500$ angstroms as the standard visual wavelength. All converted extinctions are termed visual extinctions, A_V . Reduction to visual extinctions is made by assuming a 'standard' interstellar reddening law. The conversion factors relating red and blue magnitudes to visual are given below (Dickman 1978).

$$A_V = 0.76 A_B \quad (B \cong 4300 \text{ \AA})$$

$$A_V = 1.21 A_R \quad (R \cong 6500 \text{ \AA})$$

The 'standard' reddening law has been suspect for quite some time. The possible deviations are discussed in detail in Dickman's thesis (1976).

Once the visual extinction was determined for each colour, intercomparison was possible. For our cloud we found the features present on the red and blue extinction contour maps to agree fairly well. The magnitude of the red extinction disagrees

significantly from the blue only for large extinctions ($A \gtrsim 3.5$). The visual extinction derived from the red print became increasingly higher than that for the blue star counts as A_V increased above 3.5 magnitudes. Since the red Palomar print had on average more stars per grid element the extinctions determined from the red prints for $A \gtrsim 3.5$ are probably more representative of the true value than those obtained from the blue print.

The overall uncertainty in A_V for regions where stars were counted is probably no more than one magnitude. The areas of greater extinction are a lower limit where the uncertainty is several magnitudes. The squares encompassing the HII region are particularly difficult to judge since no stars can be distinguished in the exposed areas of the Palomar prints.

A further problem that should be reconciled is the expected number of foreground stars that were counted. From the star counts on the blue print we found no evidence for the presence of more than one foreground star per grid element. Since Sharpless 222 is located off the galactic plane and 800 parsecs distant we expect few foreground stars as indicated by the blue star counts. Subtracting one star per grid element throughout the field will change the ratio between the number of stars in the reference region and the number of stars in the obscured region by a small amount. This leads to a slight underestimate of the actual extinction. In conclusion, we feel confident that the extinctions are lower limits accurate to one magnitude, except in regions where no stars were found in a grid element.

Table VI gives a summary of the results of this chapter.

Table V -Van Rhijn's Table for $b = -9.0^\circ$

The logarithm of the number of stars of all magnitudes per square degree to a limiting magnitude, m , is given under the heading $\log N_m$. This data is interpolated for $b = -9.0^\circ$ from Allen's "Astrophysical Quantities".

Table V -Van Rhijn's Table for $b=-9.0^{\circ}$

| m | log N_m | m | log N_m | m | log N_m |
|------|-----------|------|-----------|------|-----------|
| 12.0 | 1.63 | 14.4 | 2.62 | 16.8 | 3.49 |
| 12.1 | 1.67 | 14.5 | 2.66 | 16.9 | 3.52 |
| 12.2 | 1.71 | 14.6 | 2.70 | 17.0 | 3.56 |
| 12.3 | 1.76 | 14.7 | 2.74 | 17.1 | 3.59 |
| 12.4 | 1.80 | 14.8 | 2.78 | 17.2 | 3.63 |
| 12.5 | 1.84 | 14.9 | 2.82 | 17.3 | 3.66 |
| 12.6 | 1.88 | 15.0 | 2.86 | 17.4 | 3.70 |
| 12.7 | 1.92 | 15.1 | 2.89 | 17.5 | 3.73 |
| 12.8 | 1.97 | 15.2 | 2.93 | 17.6 | 3.77 |
| 12.9 | 2.01 | 15.3 | 2.96 | 17.7 | 3.80 |
| 13.0 | 2.05 | 15.4 | 3.00 | 17.8 | 3.84 |
| 13.1 | 2.09 | 15.5 | 3.03 | 17.9 | 3.87 |
| 13.2 | 2.13 | 15.6 | 3.07 | 18.0 | 3.90 |
| 13.3 | 2.17 | 15.7 | 3.10 | 18.1 | 3.94 |
| 13.4 | 2.21 | 15.8 | 3.14 | 18.2 | 3.98 |
| 13.5 | 2.26 | 15.9 | 3.17 | 18.3 | 4.01 |
| 13.6 | 2.30 | 16.0 | 3.21 | 18.4 | 4.05 |
| 13.7 | 2.34 | 16.1 | 3.24 | 18.5 | 4.09 |
| 13.8 | 2.38 | 16.2 | 3.28 | 18.6 | 4.13 |
| 13.9 | 2.42 | 16.3 | 3.31 | 18.7 | 4.17 |
| 14.0 | 2.46 | 16.4 | 3.35 | 18.8 | 4.20 |
| 14.1 | 2.50 | 16.6 | 3.38 | 18.9 | 4.24 |
| 14.2 | 2.54 | 16.7 | 3.42 | 19.0 | 4.28 |
| 14.3 | 2.58 | 16.8 | 3.45 | | |

Figures 11, 12, and 13 A_B , A_R , and A_V Extinction Contours

The magnitudes of extinction were determined using the standard procedure outlined in section III.6-Star Counting Theory, Data, and Results. The numbers on each contour map represent the interval of extinction. For example, a 4 would indicate the extinction is between 3 and 4 magnitudes. Figure 11 represents the results from the blue ($B \approx 4300 \text{ \AA}$) print of the Palomar Survey. Figure 12 gives the results from the red print ($R \approx 6500 \text{ \AA}$) and Figure 13 is the average of the preceeding figures converted to visual extinction ($V \approx 5500 \text{ \AA}$). The conversion procedure is outlined in Dickman (1978). The dashed regions represent the extent of the nebulosity as seen on each of the Palomar prints. The axis are scaled in 1.8 arcminute intervals from the centre (0.0,0.0),

$$\alpha(1950) = 04^{\text{h}}26^{\text{m}}34.^{\text{s}}0 \quad (\text{Right Ascension})$$

$$\delta(1950) = 35^{\circ}13'00.''0 \quad (\text{Declination})$$

Figure 11 -A, Extinction Contours

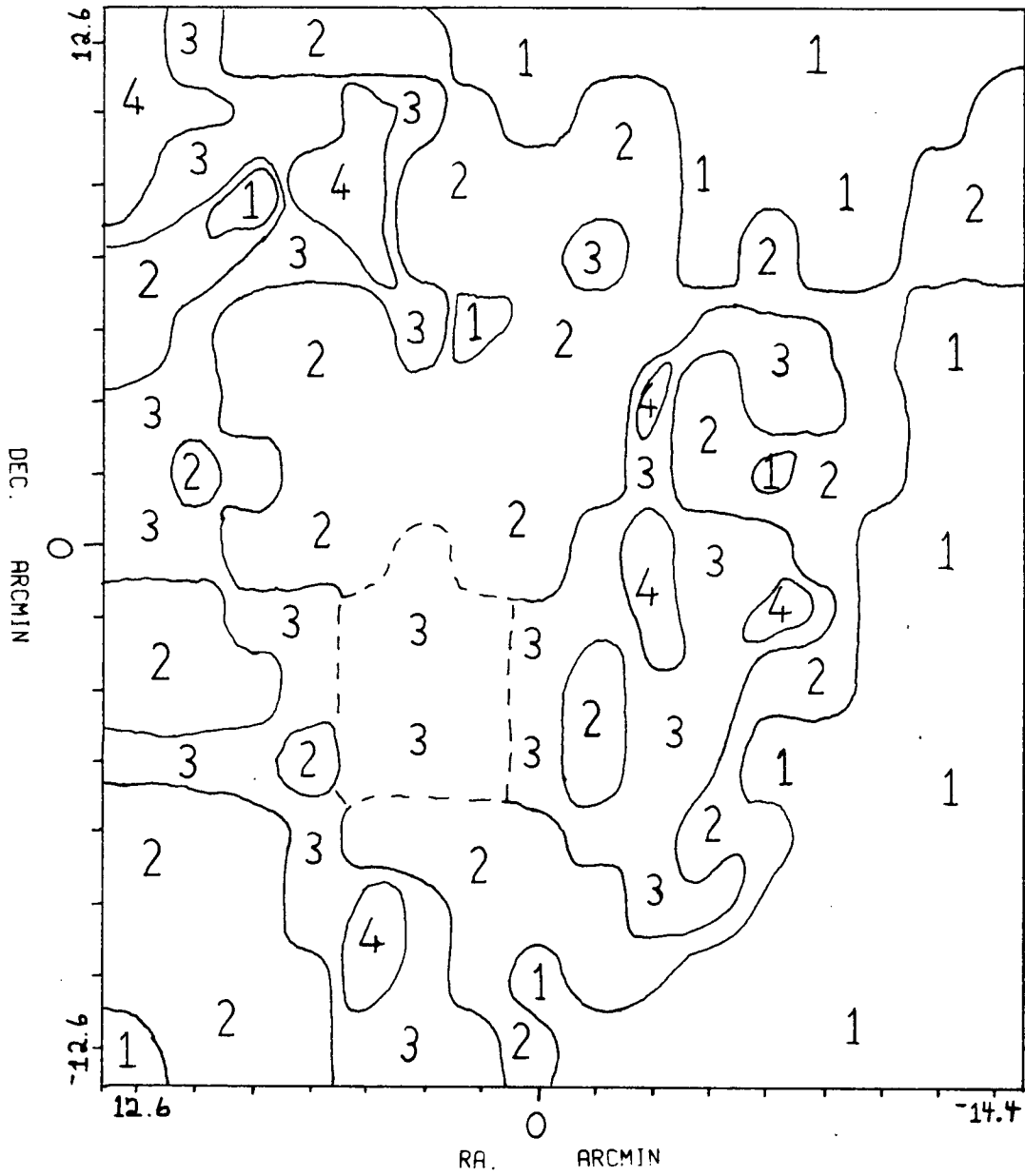


Figure 12 $-A_R$ Extinction Contours

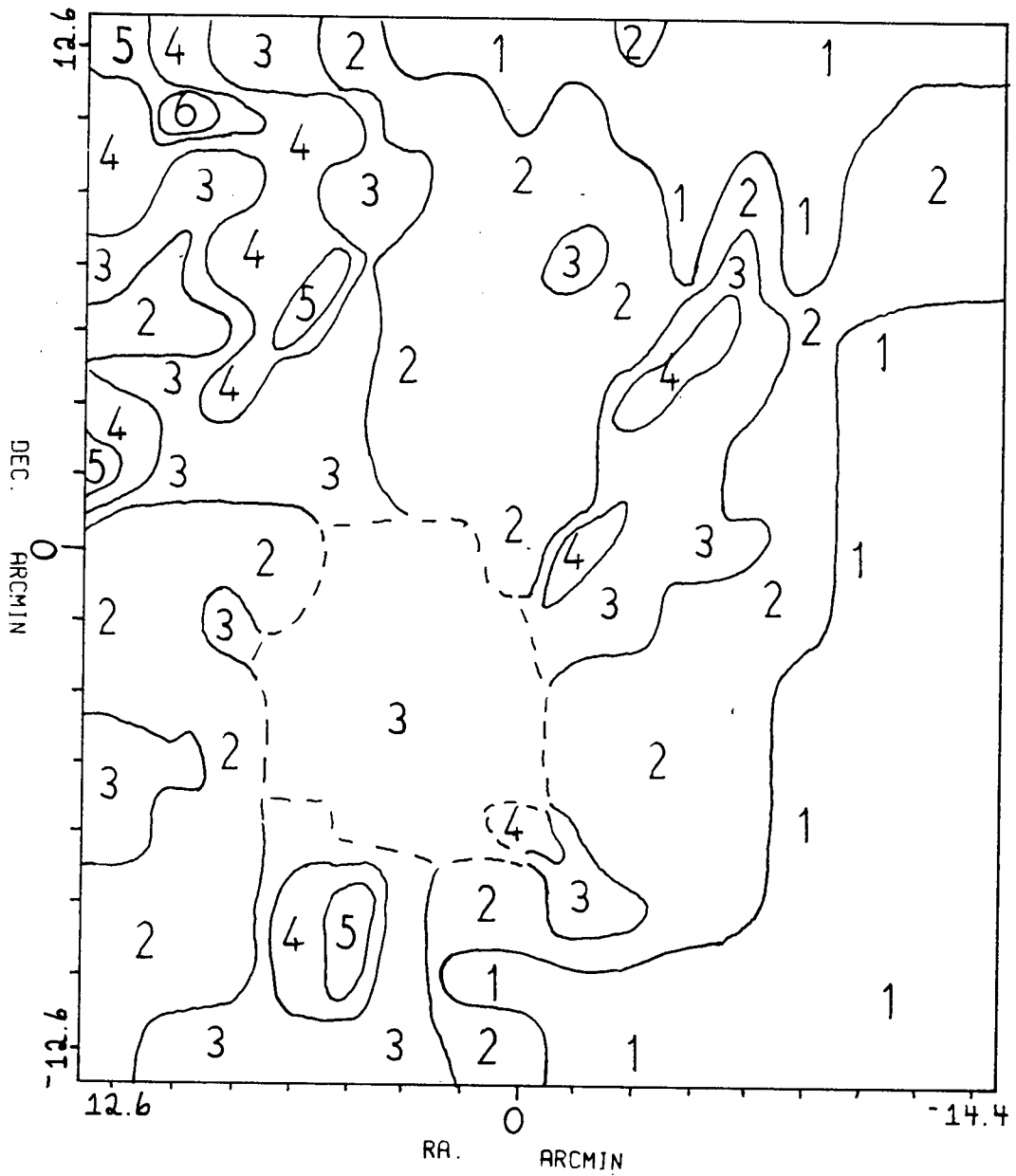


Figure 13 $-A_v$ Extinction Contours

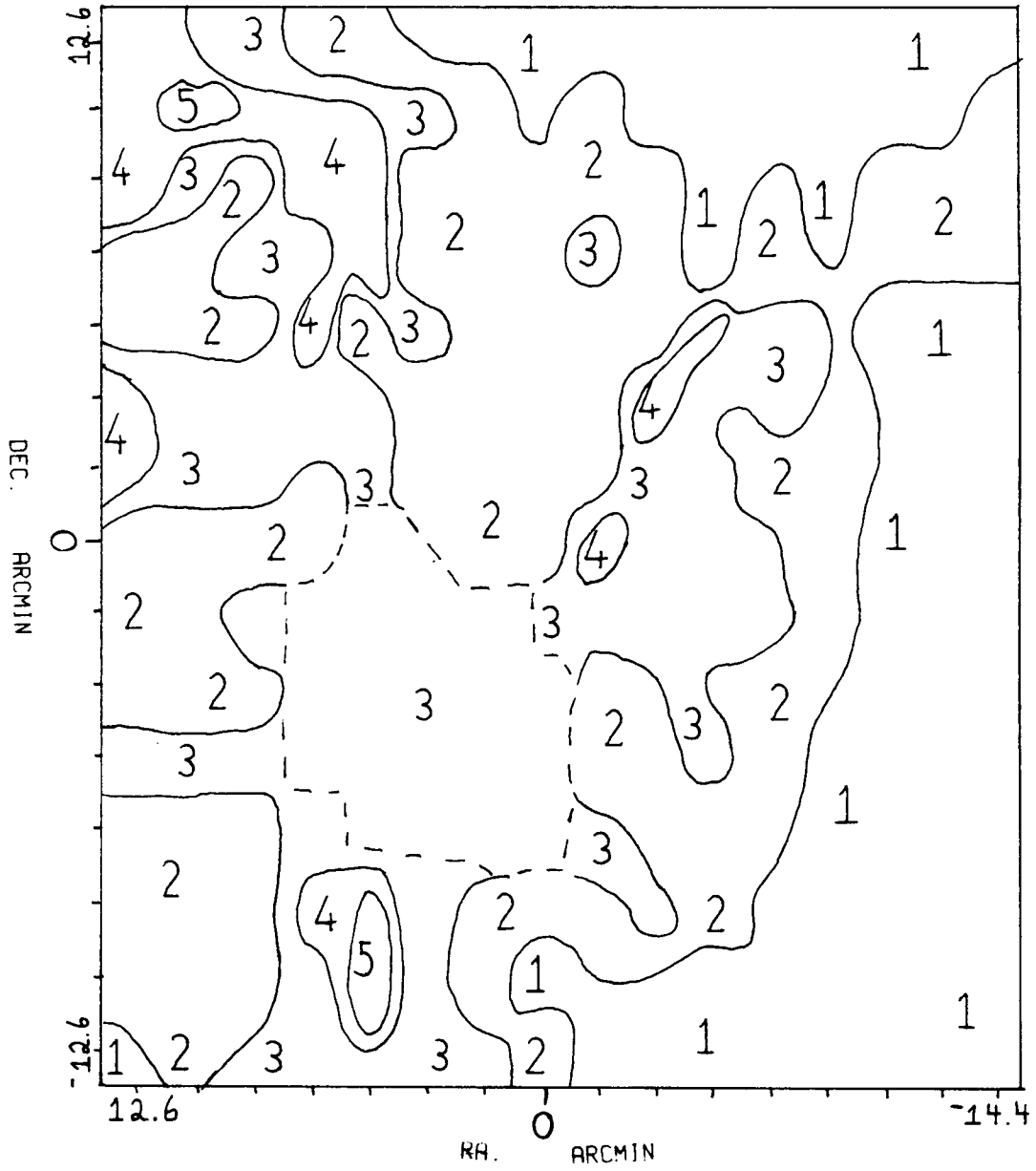


Table VI -Data Summary

Column 1 gives the coordinates of each observation. (x.x,y.y) means x.x arcminutes right ascension and y.y arcminutes declination from our nominal centre,

$$\alpha(1950) = 04^{\text{h}}26^{\text{m}}34.0^{\text{s}} \text{ (Right Ascension)}$$

$$\delta(1950) = 35^{\circ}13'00.0'' \text{ (Declination)}$$

Column 2 is the observed peak ^{12}CO radiation temperature (K) and column 3 gives the corresponding L.S.R. velocity (km s^{-1}). Column 4 gives the ^{12}CO excitation temperature (K). Columns 5 and 6 give the expected ^{13}CO profile half widths (km s^{-1}) and radiation temperature (K). The last two columns give the expected ^{13}CO opacity (nepers) and the generated ^{13}CO column density, N^{13} ($\times 10^{14} \text{ cm}^{-2}$). All of the calculations are described fully in chapter III.

Table VI -Data Summary

| Position | T_A^{12} | V | T_{ex}^{12} | ΔV^{13} | T_A^{13} | τ^{13} | N^{13} |
|---------------|------------|------|---------------|-----------------|------------|-------------|----------|
| (0.0,-14.4) | 8.5 | -1.0 | 11.9 | 1.9 | 1.2 | 0.15 | 27 |
| (0.0,-12.6) | 14.1 | -0.9 | 17.6 | 2.1 | 3.0 | 0.23 | 89 |
| (-10.8,-10.8) | 12.8 | -2.5 | 16.3 | 1.9 | 2.6 | 0.22 | 67 |
| (-9.0,-10.8) | 14.1 | -1.3 | 17.5 | 2.2 | 2.9 | 0.23 | 93 |
| (-5.4,-10.8) | 14.6 | -1.8 | 18.1 | 2.5 | 3.1 | 0.24 | 120 |
| (-1.8,-10.8) | 17.1 | -2.0 | 20.6 | 2.6 | 4.3 | 0.29 | 190 |
| (1.8,-10.8) | 13.3 | -1.1 | 16.7 | 2.5 | 2.8 | 0.24 | 99 |
| (5.4,-10.8) | 17.2 | -0.6 | 20.7 | 2.4 | 4.3 | 0.29 | 170 |
| (7.2,-10.8) | 20.8 | -0.7 | 24.3 | 2.4 | 6.3 | 0.36 | 290 |
| (9.0,-10.8) | 14.2 | -0.7 | 17.6 | 3.5 | 3.0 | 0.24 | 160 |
| (10.8,-10.8) | 11.5 | -1.6 | 14.9 | 2.2 | 2.3 | 0.22 | 69 |
| (-9.0,-9.0) | 11.5 | -1.5 | 14.9 | 2.6 | 2.3 | 0.22 | 80 |
| (0.0,-9.0) | 15.9 | -1.2 | 19.4 | 2.3 | 3.7 | 0.27 | 130 |
| (9.0,-9.0) | 14.8 | -1.0 | 18.3 | 2.0 | 3.2 | 0.24 | 97 |
| (-7.2,-7.2) | 10.4 | -1.5 | 13.8 | 2.1 | 1.9 | 0.20 | 49 |
| (0.0,-7.2) | 17.5 | -1.3 | 21.0 | 1.6 | 4.4 | 0.29 | 120 |
| (3.6,-7.2) | 14.2 | -2.4 | 17.6 | 3.1 | 3.0 | 0.24 | 140 |
| (5.4,-7.2) | 15.9 | -1.4 | 19.4 | 2.7 | 3.7 | 0.27 | 160 |
| (7.2,-7.2) | 15.4 | -1.0 | 18.8 | 2.9 | 3.4 | 0.25 | 150 |
| (9.0,-7.2) | 14.8 | -1.6 | 18.3 | 2.5 | 3.2 | 0.24 | 120 |
| (-5.4,-5.4) | 10.1 | -1.5 | 13.5 | 2.0 | 1.8 | 0.20 | 46 |
| (0.0,-5.4) | 13.6 | -1.0 | 17.1 | 2.3 | 2.8 | 0.23 | 95 |
| (3.6,-5.4) | 18.9 | -1.0 | 22.4 | 2.1 | 5.3 | 0.33 | 190 |
| (5.4,-5.4) | 13.9 | -1.1 | 17.4 | 2.8 | 3.0 | 0.25 | 120 |

| Position | T_A^{12} | V | T_{ex}^{12} | ΔV^{13} | T_A^{13} | τ^{13} | N^{13} |
|-------------|------------|------|---------------|-----------------|------------|-------------|----------|
| (7.2,-5.4) | 20.9 | -1.0 | 24.3 | 1.7 | 6.3 | 0.36 | 210 |
| (9.0,-5.4) | 13.1 | -1.3 | 16.5 | 2.0 | 2.8 | 0.24 | 78 |
| (-9.0,-3.6) | 12.5 | -2.5 | 15.9 | 1.8 | 2.5 | 0.22 | 63 |
| (-3.6,-3.6) | 11.8 | -1.9 | 15.2 | 1.9 | 2.3 | 0.22 | 54 |
| (0.0,-3.6) | 15.2 | -0.9 | 18.6 | 2.3 | 3.4 | 0.25 | 120 |
| (3.6,-3.6) | 11.3 | -2.0 | 14.7 | 2.8 | 2.2 | 0.22 | 82 |
| (5.4,-3.6) | 13.5 | -1.4 | 16.9 | 2.2 | 2.9 | 0.24 | 91 |
| (7.2,-3.6) | c.12.0 | -1.5 | 15.4 | 2.4 | 2.4 | 0.22 | 77 |
| Bad Point | | | | | | | |
| (9.0,-3.6) | 12.2 | -1.6 | 15.6 | 2.0 | 2.4 | 0.22 | 67 |
| (10.8,-3.6) | 12.6 | -1.6 | 16.0 | 1.7 | 2.5 | 0.22 | 59 |
| (-9.0,-1.8) | 11.5 | -1.8 | 15.0 | 1.6 | 2.2 | 0.21 | 47 |
| (-1.8,-1.8) | 10.5 | -2.1 | 13.9 | 2.2 | 2.0 | 0.21 | 54 |
| (0.0,-1.8) | 17.2 | -1.3 | 20.7 | 2.1 | 4.2 | 0.28 | 150 |
| (1.8,-1.8) | 8.2 | -1.1 | 11.5 | 1.4 | 1.5 | 0.20 | 25 |
| (3.6,-1.8) | 12.0 | -2.1 | 15.4 | 2.1 | 2.4 | 0.22 | 68 |
| (5.4,-1.8) | 13.8 | -1.0 | 17.2 | 2.4 | 3.0 | 0.25 | 110 |
| (7.2,-1.8) | 13.1 | -1.2 | 16.5 | 2.4 | 2.8 | 0.24 | 95 |
| (9.0,-1.8) | 15.8 | -1.0 | 19.2 | 2.1 | 3.7 | 0.27 | 120 |
| (-12.6,0.0) | 10.0 | -0.6 | 13.4 | 1.0 | 1.8 | 0.20 | 23 |
| (-10.8,0.0) | 7.7 | -1.8 | 11.1 | 1.6 | 1.3 | 0.19 | 25 |
| (-9.0,0.0) | 11.1 | -3.5 | 14.5 | 1.6 | 2.2 | 0.22 | 46 |
| (-7.2,0.0) | 12.7 | -2.1 | 16.2 | 2.3 | 2.7 | 0.23 | 85 |
| (-5.4,0.0) | 2.9 | -1.3 | 6.1 | 1.0 | 0.5 | 0.19 | 6 |
| (-3.6,0.0) | 14.5 | -1.9 | 18.0 | 1.8 | 3.1 | 0.24 | 81 |
| (-1.8,0.0) | 8.6 | -2.3 | 11.9 | 2.5 | 1.6 | 0.20 | 46 |
| (0.0,0.0) | 9.9 | -2.1 | 13.3 | 2.3 | 1.9 | 0.22 | 55 |

| Position | $T_A^{1,2}$ | V | $T_{ex}^{1,2}$ | $\Delta V^{1,3}$ | $T_A^{1,3}$ | $\tau^{1,3}$ | $N^{1,3}$ |
|------------|-------------|------|----------------|------------------|-------------|--------------|-----------|
| (1.8,0.0) | 14.0 | -1.9 | 17.5 | 2.4 | 2.9 | 0.23 | 100 |
| (3.6,0.0) | 12.3 | -0.5 | 15.7 | 2.1 | 2.5 | 0.22 | 70 |
| (5.4,0.0) | 11.1 | -2.2 | 14.5 | 2.5 | 2.2 | 0.22 | 72 |
| (7.2,0.0) | 11.3 | -1.1 | 14.8 | 2.8 | 2.2 | 0.22 | 84 |
| (9.0,0.0) | 12.8 | -0.8 | 16.2 | 2.4 | 2.6 | 0.23 | 85 |
| (10.8,0.0) | 11.0 | -2.5 | 14.4 | 2.2 | 2.1 | 0.21 | 59 |
| (12.6,0.0) | 7.4 | -0.9 | 10.8 | 2.3 | 1.2 | 0.18 | 31 |
| (-1.8,1.8) | 9.6 | -1.3 | 13.0 | 2.8 | 1.8 | 0.21 | 63 |
| (0.0,1.8) | 7.6 | -1.0 | 11.0 | 1.5 | 1.3 | 0.19 | 23 |
| (1.8,1.8) | 9.6 | -1.7 | 13.0 | 2.0 | 1.8 | 0.20 | 43 |
| (-3.6,3.6) | 11.0 | -2.1 | 14.4 | 2.1 | 2.1 | 0.22 | 59 |
| (0.0,3.6) | 7.5 | -1.7 | 10.8 | 2.0 | 1.3 | 0.19 | 30 |
| (3.6,3.6) | 9.6 | -2.2 | 13.0 | 1.7 | 1.8 | 0.21 | 37 |
| (5.4,3.6) | 10.1 | -1.1 | 13.5 | 1.9 | 2.0 | 0.22 | 46 |
| (7.2,3.6) | 13.7 | -0.2 | 17.1 | 1.1 | 2.9 | 0.24 | 44 |
| (-9.0,5.4) | 12.4 | -1.2 | 15.8 | 1.7 | 2.5 | 0.23 | 58 |
| (-5.4,5.4) | 13.2 | -0.9 | 16.6 | 2.0 | 2.8 | 0.23 | 77 |
| (-1.8,5.4) | 11.4 | -1.4 | 14.8 | 1.4 | 2.3 | 0.22 | 44 |
| (0.0,5.4) | 9.7 | -1.3 | 13.1 | 2.2 | 1.8 | 0.21 | 49 |
| (1.8,5.4) | 5.6 | -1.1 | 8.9 | 1.5 | 0.9 | 0.17 | 15 |
| (5.4,5.4) | 11.1 | -1.7 | 14.5 | 1.7 | 2.2 | 0.22 | 50 |
| (9.0,5.4) | 13.0 | -1.0 | 16.4 | 2.0 | 2.7 | 0.23 | 75 |
| (-7.2,7.2) | 12.0 | -2.0 | 15.4 | 1.7 | 2.4 | 0.23 | 55 |
| (0.0,7.2) | 15.1 | -1.1 | 18.6 | 1.4 | 3.3 | 0.25 | 68 |
| (5.4,7.2) | 13.9 | -1.4 | 17.4 | 1.7 | 2.9 | 0.23 | 74 |
| (7.2,7.2) | 13.1 | -2.3 | 16.5 | 1.8 | 2.7 | 0.23 | 69 |

| Position | T_A^{12} | V | T_{ex}^{12} | ΔV^{13} | T_A^{13} | τ^{13} | N^{13} |
|--------------|------------|------|---------------|-----------------|------------|-------------|----------|
| (-9.0,9.0) | 6.4 | -1.5 | 9.8 | 1.5 | 0.9 | 0.15 | 14 |
| (0.0,9.0) | 11.6 | -1.2 | 15.1 | 2.0 | 2.3 | 0.22 | 63 |
| (9.0,9.0) | 13.2 | -1.9 | 16.7 | 2.2 | 2.7 | 0.23 | 84 |
| (-10.8,10.8) | 5.4 | -2.1 | 8.7 | 1.2 | 0.7 | 0.15 | 9 |
| (-9.0,10.8) | 7.8 | -1.1 | 11.2 | 1.0 | 1.1 | 0.16 | 13 |
| (-5.4,10.8) | 10.0 | -0.6 | 13.4 | 1.9 | 1.7 | 0.18 | 39 |
| (-1.8,10.8) | 10.6 | -2.0 | 14.0 | 1.2 | 1.9 | 0.20 | 30 |
| (0.0,10.8) | 9.5 | -2.1 | 12.9 | 2.5 | 1.6 | 0.18 | 48 |
| (1.8,10.8) | 7.6 | -0.9 | 11.0 | 2.0 | 1.1 | 0.16 | 26 |
| (7.2,10.8) | 8.5 | -0.8 | 11.9 | 1.6 | 1.4 | 0.17 | 25 |
| (9.0,10.8) | 13.3 | -1.2 | 16.7 | 2.2 | 2.7 | 0.23 | 84 |
| (0.0,12.6) | 5.6 | -1.2 | 8.9 | 1.7 | 0.7 | 0.14 | 14 |

IV. DISCUSSION OF RESULTS

IV.1.1-Previous Observations: Introduction

Sharpless 222 appears to have been observed first by F.G. Pease (1917) as NGC 1579 Perseus. A general description and the location was given. Hubble (1922) categorized NGC 1579 as an object of size two on a scale increasing in size from one to five. Herbig (1956) suggested Lk HX101 as the probable source of illumination for NGC 1579. The photographic magnitude of Lk HX101 is 17. Herbig noted that there is a discrepancy of nine magnitudes between the observed brightness and that given by Hubble's relation connecting the apparent magnitude of the exciting star and dimensions of the nebula. He correctly explained that this problem was a result of dark lanes of material superimposed on the illuminating star, Lk HX101.

The name Sharpless 222 is derived from a list of HII regions compiled by S. Sharpless (1959). In this catalogue Sharpless 222 is described as a very bright irregular HII region with diameter six arcminutes. The location is also given.

Palomar Sky Survey prints of the region show Sharpless 222 as a small bright nebula, crossed by several obscuring dark lanes. It lies on the edge of a very long and narrow dust lane. As described by the 'Blister' Model (Israel 1977, Gilmore 1978: referred to in the INTRODUCTION), this configuration of star formation is fairly common. There are four components present in Sharpless 222: the exciting star, the HII region, the HI region, and the molecular cloud and our spatial resolution is capable of resolving only the latter two. The first two components are

treated briefly in this section.

The spectral type of the exciting star, Lk HX101, has been a matter of debate ever since Herbig (1956) classified the object as an F type star. In the last ten years most data have indicated that the spectral type is probably that of a zero age main sequence (Z.A.M.S.) B0.5 star (Allen 1973, Brown et al. 1976, Altenhoff et al. 1976, Harris 1976), where a Z.A.M.S. B0.5 type star is defined according to the parameters given by Panagia (1973). The photographic magnitude of $m_{pg} = 17$ and the distance of at least 800 parsecs (Herbig 1971) indicates there are nearly ten magnitudes of visual extinction present.

The spectrum of the point source for Lk HX101 above 5 GHz has a spectral index of one ($S_\nu \propto \nu^{-1}$, Cohen 1980) with some flattening of the spectrum between 30 and 90 GHz (Schwartz and Spencer 1977). The optical spectrum is continuous (Cohen and Kuhi 1979) and from the ratio of hydrogen lines $P\beta$ (Thompson et al. 1977) to $H\gamma$ (Cohen and Kuhi 1979), Cohen (1980) finds $A_V = 10$ magnitudes. For the point source Cohen (1980) also calculates a mass loss of $3 \times 10^{-5} M_\odot \text{ yr}^{-1}$ which corresponds well with a B0.5 Z.A.M.S. star. Cohen (1980) uses several methods to determine the visual extinction. In each case he finds the total extinction of the star to be between 9 and 10 magnitudes consistent with a B0.5 star.

Lk HX101 is a bright infrared source exciting the surrounding nebula NGC 1579 (Cohen and Woolf 1971). Cohen and Dewhirst (1970) found Lk HX101 coincident with the infrared source IRC 40091 (Neugebauer and Leighton 1969). The K magnitude appears to be near three (Grasdalen and Gaustad 1971, Allen

1973, Strecker and Ney 1974) with a colour index $I - K$ of 5.72 magnitudes (Cohen and Dewhirst 1970). The observed infrared excess and rich emission line spectrum provides evidence for both a gas and dust envelope surrounding Lk H α 101. On an unpublished print of the Steward Observatory Near Infrared Photographic Sky Survey there are about a dozen stars in the molecular cloud with at least a 2.5 magnitude colour excess. Of these, ten are within our field of observations. Table VII gives a summary of their positions and any coincidence with the CO observations. Figure 14 is a diagram of the Steward Observatory infrared print.

Lk H α 101 can thus be represented as a B0.5 star in an early phase of evolution. It seems to be losing mass at a rate of about $3 \times 10^{-5} M_{\odot} \text{ yr}^{-1}$. The evidence of mass loss rather than mass infall implies that the protostar is no longer collapsing. In all probability it has very recently reached the main sequence. As a result of the mass loss, a thick circumstellar dust shell has formed around Lk H α 101 (Simon and Dyck 1977, Cohen 1980). The dust shell is most likely responsible for producing both the high reddening and the infrared excesses present. It appears that the dust and HII regions are clumped in an asymmetric way with the HII region at the core (Thompson et al. 1976, Thompson and Reed 1976). The shell geometry permits only two per cent of the stellar ionizing photons to escape, creating a weakly ionized halo. The total extinction arising from this circumstellar shell is about 9 to 10 magnitudes. For a B0.5 star at 800 parsecs, Osterbrook (1974, Table 2.3) suggests an inner ionized region of 0.7 arcseconds and a more extended

zone of emission (32 arcseconds). These radii do agree fairly well with the observed radio picture. Spencer and Schwartz (1974) estimated the inner core was less than one arcsecond. Altenhoff et al. (1976) and Harris (1976) both narrowed the inner core size to 0.5 arcseconds. Harris further notes the existence of the more extended emission and Altenhoff et al. (1976) gives the size as 35 arcseconds based on the 5 and 10.7 GHz data. The question of the asymmetry of the nebula can be solved by assuming that the HII region is flattened. Herbig (1971) suggested that the associated nebula might in fact be elliptical in shape and have three parts obscured. Cohen (1980) suggests that the circumstellar dust actually lies in a flattened distribution, thinnest over the poles of Lk H α 101. In this way only a small fraction of the stellar flux can escape through the polar caps. This appears to be the case with the stellar radiation. This flux helps maintain the optical nebula, NGC 1579, and the observed radio halo.

The youth of the illuminating star, Lk H α 101, is supported by the early spectral type, the high infrared excesses and the high mass loss observed. Lk H α 101 appears to be an excellent candidate with which strong CO emission will be associated.

| Infrared Star | ^{12}CO contours (kelvin) | A_V extinc. (mag.) | ^{13}CO contours (kelvin) | $N_{\text{col}}(^{13}\text{CO})$ contours ($\times 10^{15} \text{ cm}^{-2}$) |
|----------------|--|----------------------------|--|--|
| #1-(13.4,5.5) | 10.0 | 0.8 | 2.8 | 8.0 |
| #2-(5.7,-13.1) | 10.0 | 2.2 | 2.3 | 6.0 |
| #3-(-2.7,-6.6) | 8.5 | 2.2 | 2.8 | 6.0 |
| #4-(-7.0,1.6) | 14.0 | 2.0 | 3.3 | 12.5 |
| #5-(-3.0,6.7) | 9.0 | 1.9 | 2.8 | 6.0 |
| #6-(2.2,-1.8) | 5.0 | 1.5 | 1.8 | 4.0 |
| #7-(3.8,-4.5) | 13.0 | 1.8 | 4.5 | 14.0 |
| #8-(3.5,-4.2) | 12.0 | 1.7 | 4.0 | 11.0 |
| #9-(4.1,-3.5) | 11.5 | 1.6 | 2.8 | 10.0 |
| #10-(4.9,-3.1) | 12.5 | 1.6 | 2.8 | 9.0 |
| #11-(5.6,-3.8) | 12.5 | 2.0 | 2.8 | 10.0 |

Table VII -Infrared Star Positions

The eleven infrared stars are listed with their positions from the centre of our observation field.

$$\alpha(1950) = 04^{\text{h}}26^{\text{m}}34.5^{\text{s}} \quad (\text{Right Ascension})$$

$$\delta(1950) = 35^{\circ}13'00.0'' \quad (\text{Declination})$$

Also given are the ^{12}CO radiation temperatures, visual extinction, expected ^{13}CO radiation temperatures, and the generated ^{13}CO column density for each of the infrared star positions. Very little coincidence between the positions of the CO hot spots and the infrared stars can be seen.

Figure 14 -Infrared Diagram

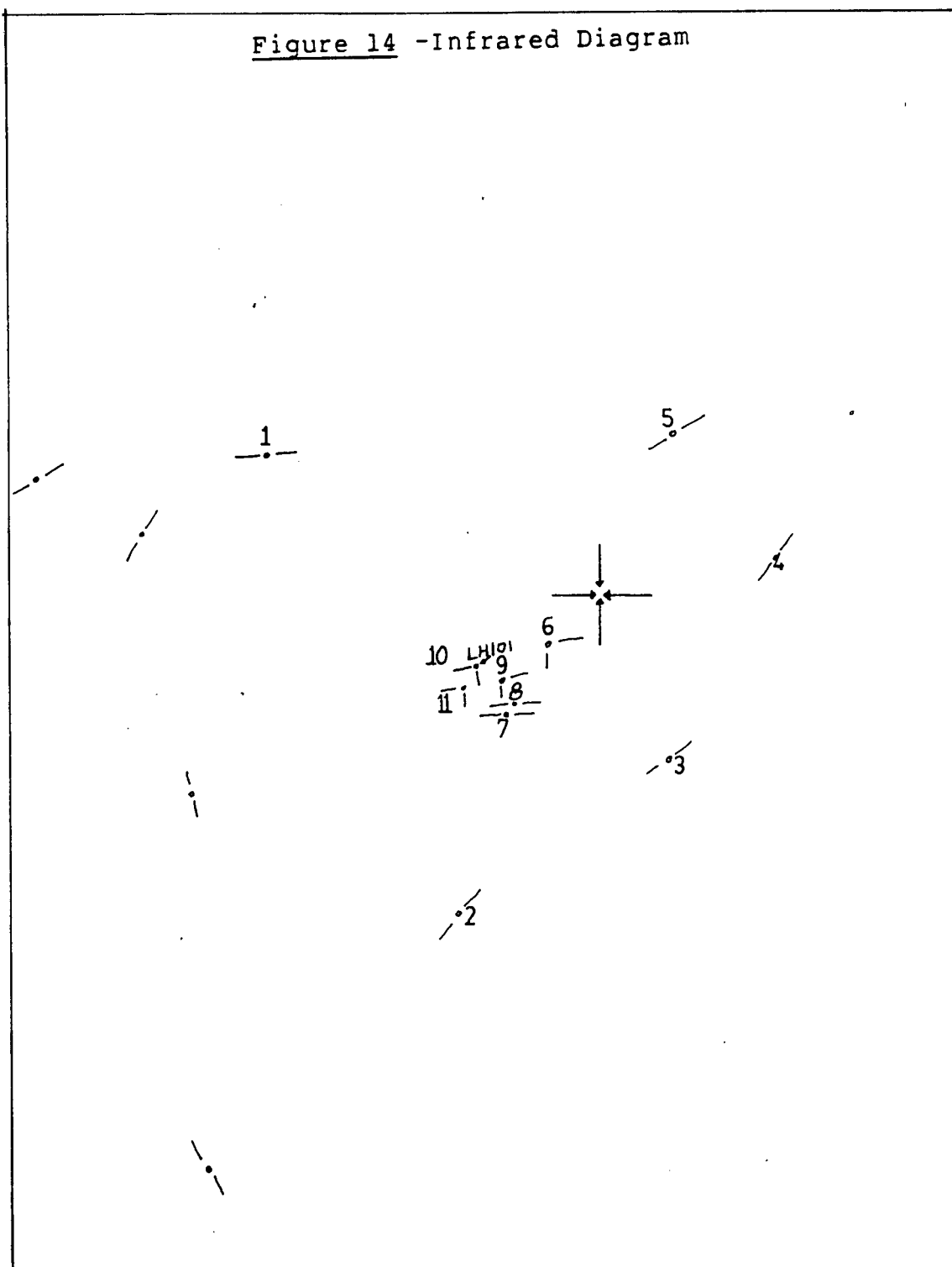
Figure 14 is a schematic representation of the infrared print (8000 to 9000 Å) reproduced by kind permission from Dr. E. Craine of the Steward Observatory. The converging arrows indicates the centre of our survey field,

$$\alpha(1950) = 04^{\text{h}} 26^{\text{m}} 34.0^{\text{s}} \quad (\text{Right Ascension})$$

$$\delta(1950) = 35^{\circ} 13' 00.0'' \quad (\text{Declination})$$

Lk H α 101 is indicated by LH101 and the other infrared stars in our observation field are numbered. The details of each are summarized in Table VII-Infrared Star Positions. The scale of the figure is 7.03 millimetres per 1.8 arcminute interval.

Figure 14 -Infrared Diagram



IV.1.2-Previous Observations: HI Results

The first twenty-one centimeter data of Sharpless 222 were obtained by Riegel (1967). He detected an HI feature which coincides exactly with Lk H α 101. He found a systematic radial velocity of 3.5 km s^{-1} and a velocity half width of 8.1 km s^{-1} .

An incomplete map of HI was obtained by Felli and Churchwell (1972). They found a maximum main beam brightness temperature of one kelvin. The peak HI temperature was located precisely at the optical coordinates. The partially sampled map is given in Figure 15.

The most complete HI data yet obtained is that of Dewdney and Roger (1981). An example of their spectra is given in Figure 16. The data were obtained using the synthesis interferometer at the Dominion Radio Astrophysical Observatory, Penticton, British Columbia. The spectra show two components in HI. The velocity of the absorption component, $0 \pm 2 \text{ km s}^{-1}$, coincides very well with the observed dip in our ^{12}CO profiles (Figure 18). The absorption component is present in all the spectra provided by Dewdney and Roger. From these spectra we see no evidence of velocity structure outside the central profile.

Figure 17 is a three dimensional display of their HI data. The front face is a map of the integrated HI with the position of Lk H α 101 indicated. As we can see Lk H α 101 is located about three arcminutes to the east of the highest HI contour centre. The two other faces indicate the HI velocity structure for constant right ascension or declination. Note that the spatial resolution used at Penticton is similar to our ^{12}CO resolution

for Sharpless 222. A full comparison of the two data sets is given in section IV.2.

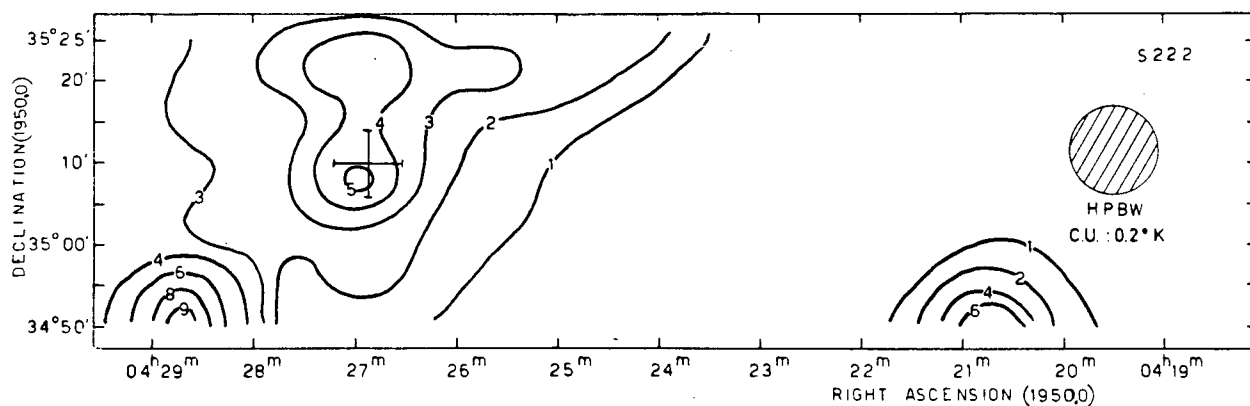


Figure 15 -HI Contour Map, Felli and Churchwell

This HI contour map of Sharpless 222 is the result of an incomplete survey by Felli and Churchwell (1972). The radio and optical coordinates coincide. This is indicated as the cross. The contour interval is 0.2 K giving a peak brightness temperature of one kelvin.

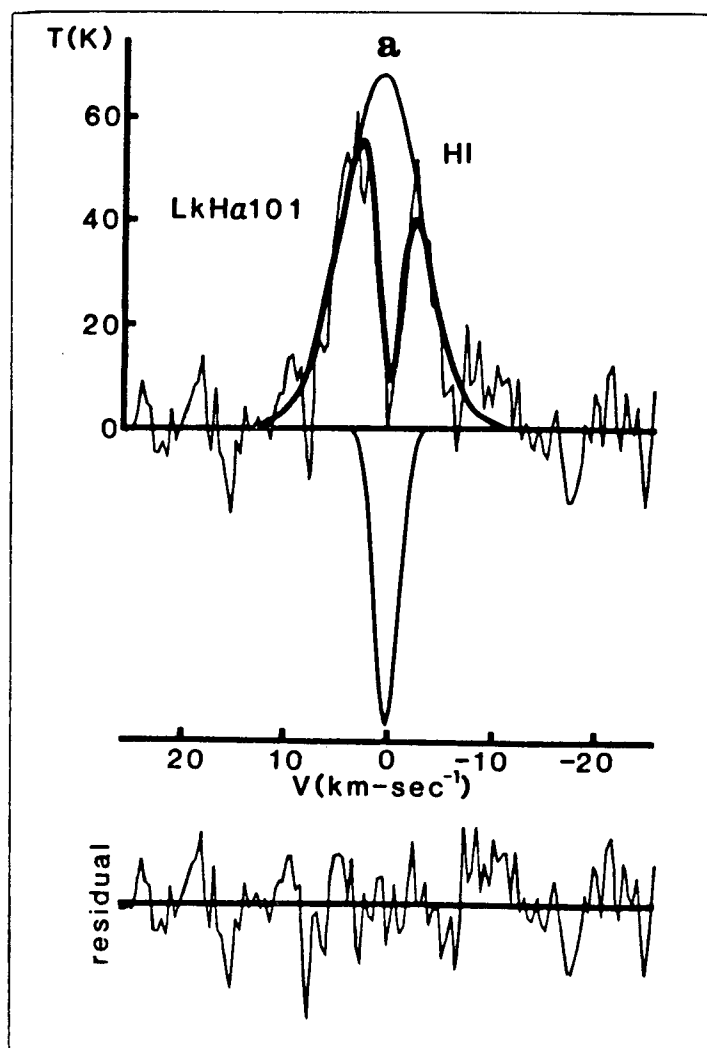


Figure 16 -HI Profile, Dewdney and Roger (1981)

This is a representative HI profile from Dewdney and Roger (1981). The figure shows the two component spectral fits. This spectra is that of Lk H α 101 (5.4,-3.6). The individual components in emission and absorption are shown in light lines, and the fitted result in heavy lines superimposed on the measured spectrum. The residual is shown below.

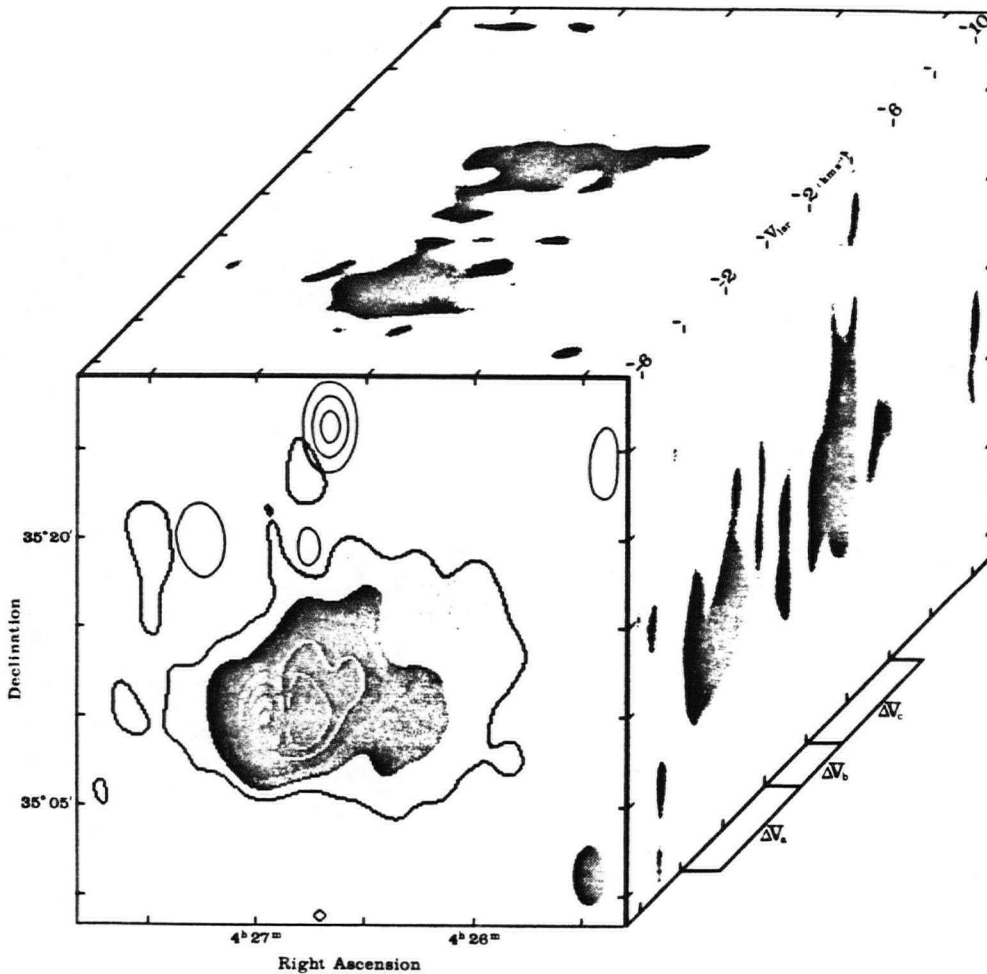


Figure 17 -3-D Synopsis of the HI results

This is a three dimensional representation of the HI emission association with Sharpless 222. The shaded contours show HI emission integrated over the velocity range -6 to $+10$ km s^{-1} . The contour steps correspond to intervals of $1.5 \times 10^{20} \text{ cm}^{-2}$ in column density. Superimposed is a contour map of continuum emission showing the source associated with Lk H α 101 (white star). Contour levels are 20, 70, 120 and 170 millijansky. The synthesized beam is shown in the lower right corner. Coordinates are for epoch 1950. The side projections are integrated over the full right ascension (RA) and declination (DEC) ranges displayed on the front face. (Dewdney and Roger 1981).

IV.1.3-Previous Observations: CO Results

As we have indicated in section IV.1.1 Lk H α 101 appears to be a young and very luminous star. CO emission, along with other molecular emission and masers, generally indicates regions of ongoing star formation. As a consequence one expects the region around Lk H α 101 to be a good source of CO emission.

To date no OH or H₂O masers have been detected in the Lk H α 101 vicinity (Turner 1971, Blitz and Lada 1979). ¹²CO emission in Sharpless 222 was first detected by Wilson et al. (1973). Only one spectrum was taken. They found an extended source (2 arcminutes) with a central velocity of $0 \pm 2 \text{ km s}^{-1}$. The profile half width was rather large, $7 \pm 2 \text{ km s}^{-1}$. The peak antenna temperature was $1.5 \pm 0.3 \text{ K}$. They also noted the presence of ¹²CO emission in the wings of their profile. The velocity of this feature was $+12 \text{ km s}^{-1}$.

The first survey of Sharpless 222 with ¹²CO was done by Knapp et al. (1976). Two positions were also observed in ¹³CO. The region studied corresponds to only a very small section of our survey centre on Lk H α 101. We estimate that about seven of our spectra cover the extent of Knapp's (1976) work. Their spectra show the same extended velocity features as those of Wilson et al. (1973). This irregularly distributed structure did not allow analytic treatment and nothing further is said about it by Knapp et al. (1976).

Figure 1 of Knapp et al. (1976) shows the Lk H α 101 profile as the brightest with a significant temperature drop as one proceeds away from this centre. The velocity of the profiles

shown in Figure 2 is approximately $-1 \pm 1 \text{ km s}^{-1}$. This velocity is representative of all of their profiles. Several of their profiles show a distinct dip at 0 km s^{-1} . They attribute this dip to self absorption. The distribution of the dips agrees with that of the dust lanes crossing the face of Sharpless 222. Figure 18 is an example of our spectra showing the dip. Knapp et al. (1976) also claim that the self absorption is responsible for the sharp drop in the ^{12}CO radiation temperatures.

Section IV.2 compares our data to that of Knapp et al. (1976), noting the many differences as well as the similarities.

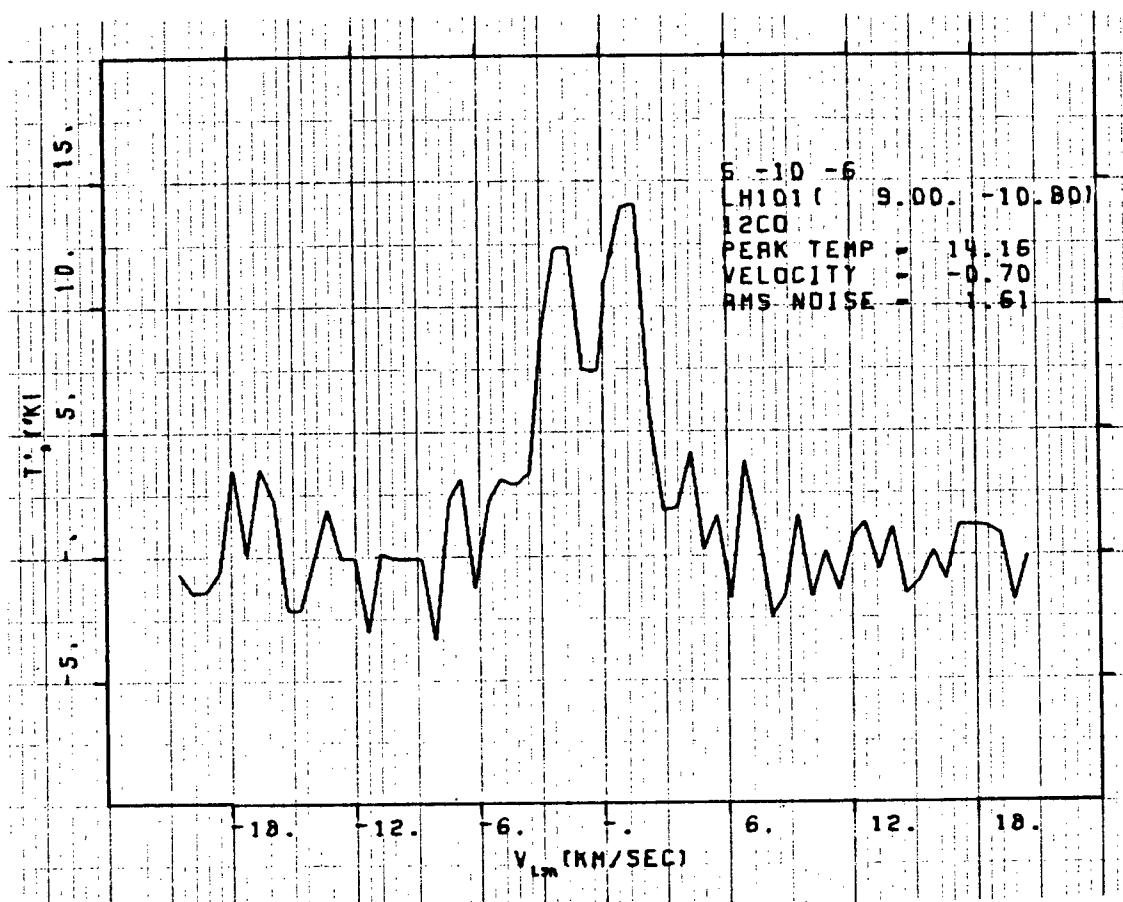


Figure 18 $-^{12}\text{CO}$ Profile Dip

This figure is representative of the ^{12}CO profiles exhibiting the prominent dip in the spectral line. Approximately 30 per cent of our positions indicated the presence of this dip. These positions appeared to be randomly oriented and did not appear to be related to dark lanes. Since the dips are not well resolved and the spectral positions are randomly distributed we could not do a proper velocity analysis.

IV.2-Our Observations

Of the four components outlined in the previous section we have covered the first two in detail. Lk HX101 appears to be an early type star, probably B0.5, with a small associated HII region. From the radio observations the size of the HII region is less than one arcsecond. Surrounding the HII region is a more extended area of fainter emission of radius 32 arcseconds. This section covers the details of the two larger components. They are the HI cloud and the molecular cloud.

Figure 19 shows an enlarged red Palomar print. Plastic overlays of the results of this project and Dewdney and Roger's (1981) HI data are located in the envelope on the back jacket of the thesis. The centre of each overlay is indicated with a cross. All of the overlays are drawn to the same scale as the photograph in Figure 19 and may be positioned with the aid of the four guide stars indicated. A full discussion of the results is given below.

Palomar prints show an exciting star, Lk HX101, surrounded by the nebula NGC 1579. The central bright nebula is approximately five arcminutes across. Fainter emission to about six arcminutes from the centre surrounds the nebula. The HII region is embedded in a very long obscuring cloud of angular extent three degrees. The average visual extinction of this elongated molecular cloud is about two magnitudes. A star count analysis indicates small 'pockets' of strong visual extinction. The maximum visual extinction measured is at least five magnitudes. Using the ratio of H atoms to visual extinction, A_V ,

from Bohlin et al. (1978) one would infer a mean total hydrogen column density of 4×10^{21} atoms cm^{-2} with 'pockets' up to 10×10^{21} atoms cm^{-2} . Table VIII at the end of this section lists A_v results derived from the generated ^{13}CO column densities for each of the clouds (Dickman 1978, Bohlin et al. 1978). The visual extinction from the ^{13}CO range from 8 to 15 magnitudes. This is in excellent agreement with the value of 11 magnitudes obtained by Dewdney and Roger (1981) but not in agreement with our calculations of the visual extinction from the star counts. The extinctions from the star count analysis are probably too low.

Our ^{12}CO observations indicate a line velocity of -1.25 km s^{-1} with a half width of 2 km s^{-1} . The profiles are sharper and narrower than a gaussian profile. Our velocity corresponds exactly with that found by Knapp et al. (1976) and Wilson et al. (1973). This is also true for the velocity half width. In approximately thirty per cent of our profiles there is a distinct dip in the profile centre at 0 km s^{-1} (Figure 18). Knapp et al. (1976) note the presence of this dip in two of their spectra and on this basis they claim that the dip is the result of self-absorption of the ^{12}CO emission in dark lanes that cut across the face of Sharpless 222. We find there is no correlation between the ^{12}CO dip and the presence of dark lanes. These profile dips are distributed quite randomly throughout our spectral positions and so analysis of the spectra in terms of two velocity components is not possible. Dewdney and Roger (1981) found no evidence for different velocity components in HI and suggest self-absorption as the cause for the profile dips.

Astronomers often make simplifying L.T.E. assumptions in determining excitation temperatures and column densities, often without adequate justification. A non local thermodynamic equilibrium (non L.T.E.) radiative transfer program, developed by Hobbs and Shuter (1981) from Bernes' (1979) Monte Carlo method, shows that the dips in the profiles are a consequence of the different assumed conditions of non L.T.E. as opposed to L.T.E. Hobbs and Shuter (1981) find pronounced dips that decrease from a maximum dip in the profile at the cloud centre to no dip at the outskirts of the cloud. Our velocity resolution is not fine enough to support this conclusion. We do find the dips more often at the cloud centres but cannot say this is a consequence on non L.T.E. conditions since these dips may just be noise on top of the profiles. We also find a few profiles on the edge of the cloud that have dips. Profile dips at the cloud edge are predicted using models with a more complicated geometry within the cloud. At present, the program is still in the developmental stage. With better velocity resolution and better signal to noise one should be able to distinguish between noise and real features such as these dips.

Our peak radiation temperature was 20 ± 2 K. Our signal to rms noise ratio averaged between eight and ten for spectra with an observed signal. The velocity half width decreased slightly from 2.5 to 1.5 km s⁻¹ towards the edge of the observation field.

The ¹²CO radiation temperature distribution can be described as a warm background (10 K) with a fragmented hot

cloud southeast of Lk H α 101. Several regions of cool gas (5 K) are located adjacent to the hot cloud (Figure 7). When the ^{12}CO velocity half width is combined with the $T_A^*(^{12}\text{CO})$ in a column density calculation, the hot and cold spots are more clearly distinguished. This is illustrated by the $N_{\text{COL}}(^{13}\text{CO})$ contours (Figure 10).

The generated ^{13}CO radiation temperature distribution described in section III.4 (Figure 10) shows the same features as ^{12}CO (Figure 7). Due to the nature of the $T_A^*(^{12}\text{CO})$ to $T_A^*(^{13}\text{CO})$ ratio the features present in the ^{13}CO contour map are clearer since the ratio emphasizes ^{12}CO hot spots. Any feature on the ^{13}CO map but not present in ^{12}CO is not resolved.

The ^{13}CO column density, $N_{\text{COL}}(^{13}\text{CO})$, combines the clarity of $T_A^*(^{13}\text{CO})$ with the variation of the half width of ^{12}CO , $\Delta V(^{12}\text{CO})$. The net result is three well resolved fragments and possibly two others inside a broad region of cooler molecular material (Figure 10).

There is a crucial difference between our results and those of Knapp et al. (1976). They observe a drastic temperature decline away from their centre (Lk H α 101). We do not observe this decline. Our observations indicate a general background of CO emission with several hot and cold clumps.

Examination of the ^{12}CO and ^{13}CO contours reveals two peculiar cold regions located at Lk H α 101 (-5.4,0.0) and Lk H α 101 (1.8,5.4). The latter is a wider region of reduced emission that is partially overlapped by an area of decreased visual extinction, A_V , northwest of the peak HI. The former, Lk H α 101 (-5.4,0.0), is a single spectrum with no detected ^{12}CO .

Surrounding spectra have moderate emission present. At first, we suspected that this might be the result of instrumental problems. However, the receiver system appeared to be working well since three other profiles collected at the same time showed significant ^{12}CO signal. Therefore, this position probably has no ^{12}CO present. Two explanations are possible. Either there is no ^{12}CO emission in a long cylindrical hole through the entire cloud or a very cool foreground cloud is absorbing the emission. The star counts were repeated in the vicinity of Lk H α 101 (-5.4,0.0) using a smaller resseau grid. There is slight evidence of a very small obscuring cloud below the resolution of our CO observations and the original star counts. From both Palomar prints no stars were recorded around this position. The integrated ^{12}CO temperature contours do not show the presence of the hole and Dewdney and Roger (1981) do not find any anomaly in their HI results at Lk H α 101 (-5.4,0.0). Consequently, we have to regard this feature as unresolved. What is required is a smaller telescope beam width to map the region.

Both Wilson et al. (1973) and Knapp et al. (1976) found velocity structure in the wings of the central profile. We found no evidence for this structure in our results. Our temperature resolution probably precluded seeing this structure. From Knapp et al. (1976) the peak temperature of the structure is very close to the noise of our spectra. The structure is also on the edge of the spectrometer range where a quadratic baseline fit was made.

The T_A^* (^{13}CO) and $\Delta V(^{13}\text{CO})$ values from Knapp et al. (1976) support the findings for other Sharpless regions by Sewall

(1980). Sewall (1980) found the ratio $T_A^* (^{12}\text{CO})$ to $T_A^* (^{13}\text{CO})$ was generally about five. The results of Knapp et al. (1976) for their two spectra for Sharpless 222 confirm this. Furthermore, Sewall (1980) found the ^{13}CO profiles mimicked the shape of the ^{12}CO profiles and $\Delta V(^{12}\text{CO})$ was approximately 1.5 times wider than $\Delta V(^{13}\text{CO})$. This agrees with the results of Knapp et al. (1976).

Why do the ^{13}CO profiles mimic the ^{12}CO profiles? A possible reason is that the ^{13}CO line is partially saturated. Sewall (1980) found the optical depth for the ^{13}CO was at least one in the case of Sharpless 152. It must be remembered that this is a lower limit for the ^{13}CO optical depth. As a result, it could be natural to observe similar line shapes for ^{12}CO and ^{13}CO if they are both saturated transitions, although this is not a necessary prerequisite for the ^{12}CO and ^{13}CO lines to be similar. Another related problem is the determination of the ^{13}CO excitation temperature. Normally, $T_{\text{ex}}(^{13}\text{CO})$ is taken to be the same as $T_{\text{ex}}(^{12}\text{CO})$. If the excitation temperatures were different for the two isotopic species then for the cooler regions the two profiles would be drastically different from each other. This is the case for cold dark globules. For warmer regions such as we have, the two profiles are similar since both lines could be saturated.

The infrared photograph from the Steward Observatory (Figure 14) shows there is very little coincidence between infrared stars and CO hot spots. One interesting feature did become apparent. Surrounding our 13 K ^{12}CO contour are three sets of infrared stars. They are infrared stars #2, #3, and the

six stars surrounding Lk H α 101. This interesting coincidence appears to agree with predictions of the 'Blister' model (Israel 1977, Gilmore 1978). In this model OB associations form just inside the surfaces of long molecular clouds. Star formation is initiated on one side of the giant cloud and proceeds into the cloud. The CO hot spots would then be the next generation of star formation. Similar but far more quantitative results were derived using numerical models for HII regions in the Champagne model (Tenorio-Tagel 1979).

In Sharpless 222 there are probably three generations of stars. Lk H α 101 is the initiating star. Habing and Israel (1979) would classify Lk H α 101 as the fourth stage in their evolutionary sequence. The other infrared stars are the next generation which could be classed as the first stage of the same sequence. The CO hot spots are the most recent stage that precedes star formation.

Dewdney and Roger's (1981) peak HI contours and the six infrared stars around Lk H α 101 are coincident. The other infrared stars appear to have no relation to the HI data. Comparing the CO and HI global features there is an anticorrelation between the two. The peak HI contours lie to the northwest of the CO hot spots. This indicates the two studies are mapping different regions. The HI velocity half width is much larger than the ^{12}CO which could be explained by the difference between the CO and HI particle masses.

The visual extinction contours show a reasonable correlation between the higher A_V and CO warm regions. This is in agreement with the work of Dickman (1978) and Frerking et al.

(1981). The peak HI emission occurs in regions where the visual extinction is lower than average. The exciting star has presumably been able to dissociate H_2 into HI to the northwest where A_V is lower. Dewdney and Roger (1981) have modeled this asymmetry quite well by assuming a steep discontinuity of density near Lk H α 101 to the east.

Dewdney and Roger (1981) find the peak column density for HI is 13×10^{20} atoms cm^{-2} and a total mass of HI of $85M_\odot$. Both estimates must assume the emission cloud is optically thin. Sewall (1980) found that the optical depth was quite high ($\tau \gtrsim 1$) for Sharpless regions and so the assumption by Dewdney and Roger (1981) may not be a good one.

Dewdney and Roger (1981) also make a rough estimate for the peak ^{13}CO column density using the results of Knapp et al. (1976). They find $N_{col}(^{13}CO)$ is 2.8×10^{16} cm^{-2} with a corresponding H_2 column density of 2.1×10^{22} atoms cm^{-2} and a visual extinction of eleven magnitudes. This value of A_V is well within other estimates already cited.

Our results suggest peak ^{13}CO column densities exactly the same as Dewdney and Roger (1981) have found from Knapp et al. (1976). Using the same analysis as used by Dewdney and Roger (1981), the peak HI column density implied from our generated ^{13}CO data would be 1.4×10^{21} atoms cm^{-2} . This is precisely that found by Dewdney and Roger (1981). The value of the visual extinction implied from our ^{13}CO results for each of the clouds is between 8 and 15 magnitudes (Table VIII). These values of A_V are well within other estimates (Thompson et al. 1977, Cohen 1980).

Finally, one can calculate the mass of each of the cloud fragments from their size and the generated ^{13}CO column density. The cloud size is defined as the width to half power of our generated ^{13}CO radiation temperature, $T_A^*(^{13}\text{CO})$, contours. A mass using the virial theorem can be computed by assuming the cloud fragment is in equilibrium, supported by turbulence, or by assuming a free fall collapse with $V \propto r$. Both give,

$$M_{\text{VIR}} \cong \frac{R \Delta V^2}{G} \quad (\text{EVANS } 1981)$$

where R is the cloud radius and ΔV is the line half width of the ^{13}CO profiles. Note that the virial mass is only a very rough estimate required for stability of the cloud. It is probably an upper limit. The generated ^{13}CO column density can also be used to estimate the cloud mass. Then,

$$M_{^{13}\text{CO}} = \frac{2}{3} (A \cdot N) \times m_H \mu$$

where A is the projected area, m_H is the atomic hydrogen mass (1.67×10^{-24} grams), μ , is the mean molecular weight (2.33 atomic mass units), X is the ratio of H_2 to ^{13}CO from Dickman

(1978), and N is the ^{13}CO column density. If N varies significantly over the extent of the cloud, $A \cdot N$ should be replaced by a sum of the $A \cdot N$ over the cloud area. The projected area, A , is poorly defined and depends on d^2 , where d is the distance. As a result, the uncertainties in the mass are large. Generally, the masses are underestimated. Tables IX and X give a summary of the clouds and their masses calculated by both methods. The masses obtained by the two methods differ significantly. The true mass of each cloud fragment is probably a compromise between the two estimates. The work of Frerking et al. (1981) probably gives the best masses for these warm clouds since their results have considered the problem of CO isotope fractionation.

The ^{13}CO column density, $N_{\text{COL}}(^{13}\text{CO})$, enables one to calculate the total molecular column density, N , using the Dickman (1978) ratio of H_2 to ^{13}CO . This is easily converted to total atomic hydrogen density and visual extinction. The results are given in Table VIII. The visual extinctions found from the star counts give results much lower than those from the column densities. Due to the large uncertainties in the star counting one should not rely too heavily on those results. The visual extinctions determined from the star counts are probably far too low whereas those found using the generated ^{13}CO column densities are likely upper limits. We feel the true value of the visual extinction, A_V , is fairly close to those given by the ^{13}CO analysis.

One final calculation was made to determine the maximum relative velocity difference between clouds if they were in

Keplerian orbits about each other. Clouds #1 and #2 located at Lk H α 101 (7.2,-10.8) and Lk H α 101 (0.0,-10.8) were chosen since they would give the largest relative velocity difference. They are the most massive and nearest neighbours. From the ^{13}CO column density mass, the velocity difference is at most 0.35 km s^{-1} . This is below the spectrometer velocity resolution. It is interesting to note that the observed difference was 0.4 km s^{-1} . Since the velocity differences expected are below our velocity resolution no further conclusions on this aspect of the clouds are possible.

Table VIII -Peak $N_{\text{col}}(^{13}\text{CO})$ and Related A_V

For each of the five clouds the peak ^{13}CO column density is given. The total H_2 column density and corresponding visual extinction are calculated. The last column gives the measured visual extinction from the star counts of the Palomar prints. $N_{\text{col}}(2\text{H}_2)$ was found using Dickman's (1978) ratio,

$$N_{\text{col}}(\text{H}_2) = (5.0 + 2.5) \times 10^5 N_{\text{col}}(^{13}\text{CO})$$

Then an estimate of the visual extinction, A_V , was determined using,

$$\langle N(\text{H}_1 + \text{H}_2)/E(\text{B-V}) \rangle = 5.8 \times 10^{21} \text{ atoms cm}^{-2} \text{ mag}^{-1}$$

(Bohlin et al. 1978) and $A_V = 0.76A_B$.

Frerking et al. (1981) have derived a larger value for the H to ^{13}CO abundance, namely 1.0×10^6 . This is twice the Dickman (1978) result and gives column densities twice as large as those indicated above. The Frerking ratio (1981) takes into account the carbon monoxide isotope fractionation.

| Cloud | Generated $N_{\text{CO-L}}(^{13}\text{CO})$ ($\times 10^{1.4} \text{ cm}^{-2}$) | $N(2\text{H}_2)$ ($\times 10^{2.2} \text{ cm}^{-2}$) | A_V | A_V star counts |
|----------------|---|---|-------|-------------------------|
| #1-(7.2,-10.8) | 287 | 2.9 | 15.5 | 4.0 |
| #2-(0.0,-10.8) | 271 | 2.7 | 14.6 | 1.5 |
| #3-(7.2,-5.4) | 205 | 2.1 | 11.0 | 2.4 |
| #4-(3.6,-5.4) | 193 | 1.9 | 10.4 | 2.2 |
| #5-(0.0,-1.8) | 147 | 1.5 | 7.9 | 2.9 |

| Cloud | ¹³ CO Size 3.5 k 3.0 k | | Mass M _☉ | Density (x10 ⁵) amu/cm ³ |
|---|---|------|------------------------|---|
| #1-(7.2,-10.8) | 186 | 3000 | 420 | 1.2 |
| #2-(0.0,-10.8) | 160 | | 530 | 1.9 |
| #3-(7.2,-5.4) | 108 | | 160 | 1.1 |
| #4-(3.6,-5.4) | 58 | | 180 | 2.9 |
| #5-(0.0,-1.8) | 27 | 230 | 128 370 | 6.7 |
| Note: 1 = 1.67 x 10 ³⁴ cm ² area for the ¹³ CO size. | | | | |

Table IX -Virial Cloud Masses

Table IX indicates the size of each cloud contained within two different ¹³CO radiation temperature contours and the corresponding virial mass assuming spherical symmetry. The average density is given in the last column of the table.

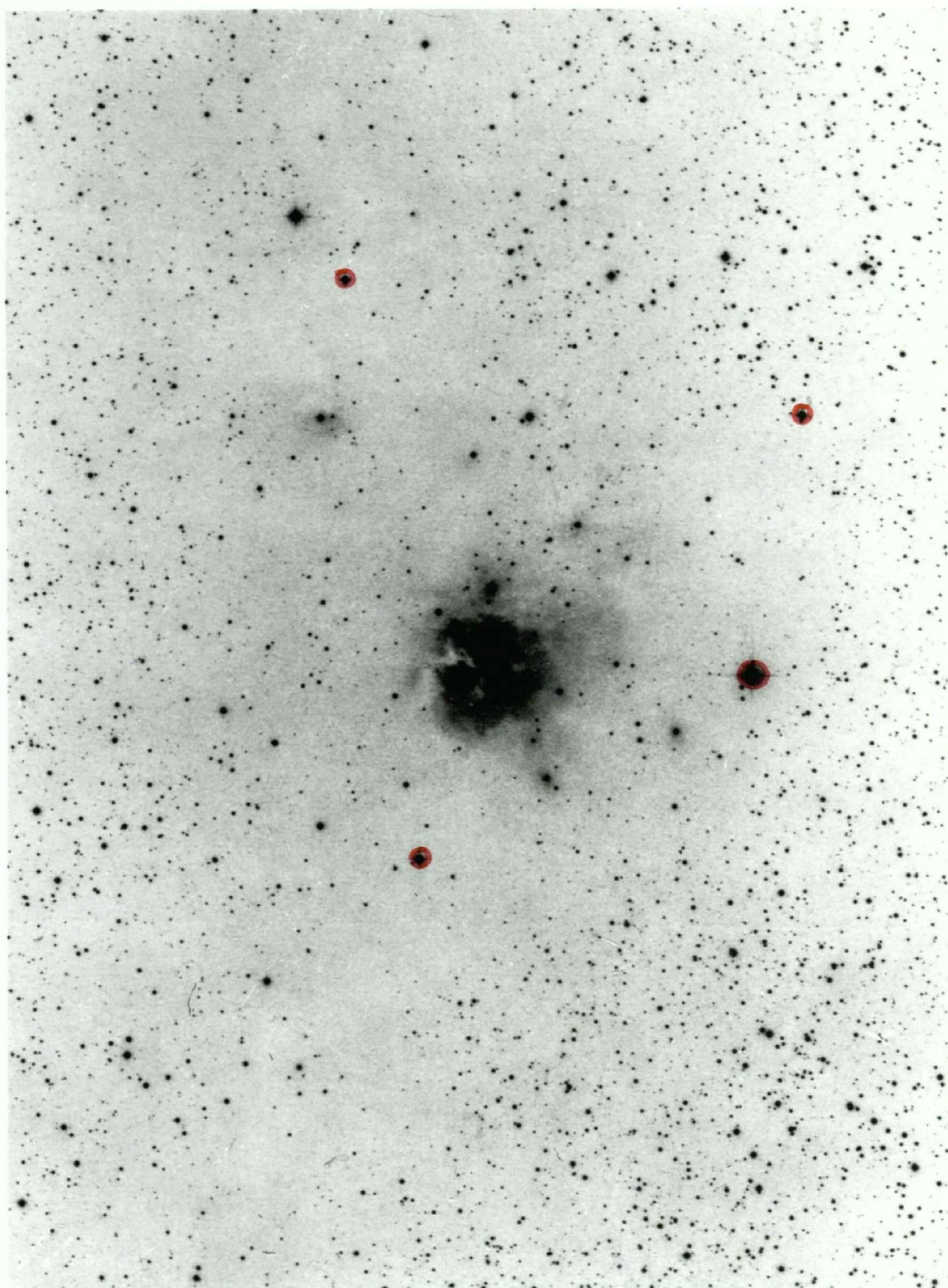
| Cloud | N (^{13}CO) Size ($\times 10^{15} \text{ cm}^{-2}$) | | | Mass M_{\odot} | Density ($\times 10^4$) amu/cm^3 |
|--|---|------|------|---------------------|---|
| | >15 | 12.5 | 10 | | |
| #1-(7.2,-10.8) | 241 | 1730 | 2490 | 49 | 1.0 |
| #2-(0.0,-10.8) | 186 | | | 41 | 1.2 |
| #3-(7.2,-5.4) | 128 | | | 25 | 1.2 |
| #4-(3.6,-5.4) | 59 | | | 11 | 1.8 |
| #5-(0.0,-1.8) | ? | 19 | 218 | ? ? 25 | 0.7 |
| Note: 1 = $1.67 \times 10^{14} \text{ cm}^2$ area for the $N_{\text{col}}(^{13}\text{CO})$ size. | | | | | |

Table X - $N_{\text{col}}(^{13}\text{CO})$ Cloud Masses

This table gives the size of each cloud contained within three different ^{13}CO column density contours and the corresponding ^{13}CO column density mass. The average density is given in the last column of the table. Frerking et al. (1981) have derived a larger value for the H_2 to ^{13}CO abundance, namely 1.0×10^6 . This is twice the Dickman (1978) result and gives column density masses twice as large as those indicated above. The Frerking ratio takes into account the problem of CO isotope fractionation.

Figure 19 - Comparison of ^{12}CO , HI, A_V etc.

Figure 19 is an enlargement of the red Palomar print.
The scale size is 6.27 millimetres per 1.8 arcminute interval.



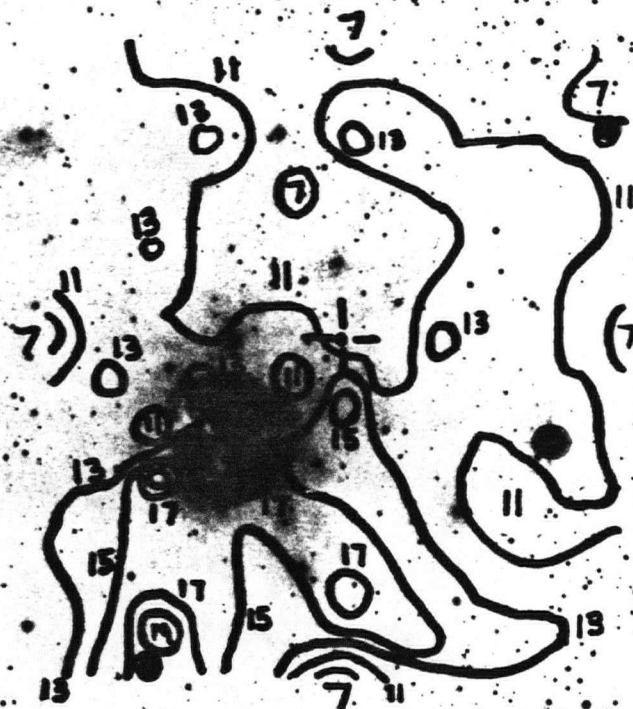


Figure 7 -Integrated ^{13}CO Contours

The $T_A^* (^{13}\text{CO})$ is integrated over all velocities to give Figure 7. The declination (DEC) versus right ascension (RA) plot shows five CO hot spots located at $(7.2, -10.8)$, $(0.0, -10.8)$, $(7.2, -5.4)$, $(3.6, -5.4)$, and $(0.0, -1.8)$.

The centre $(0.0, 0.0)$ is,

$$\alpha(1950) = 04^{\text{h}}26^{\text{m}}34^{\text{s}}.0 \quad (\text{Right Ascension})$$

$$\delta(1950) = 35^{\circ}13'00''.0 \quad (\text{Declination})$$



Figure 9 -Generated T_A^* (^{13}CO) Contours

The T_A^* (^{13}CO) contours are generated from ^{13}CO observations. The contour units are one kelvin steps. The declination (DEC) verses right ascension (RA) plot shows the same five CO hot spots present in Figure 7 (T_A^* (^{13}CO) Contours). The centre (0.0,0.0) is,

$$\alpha(1950) = 04^{\text{h}}26^{\text{m}}34^{\text{s}}.0 \quad (\text{Right Ascension})$$

$$\delta(1950) = 35^{\circ}13'00''.0 \quad (\text{Declination})$$



Figure 10 Generated $N_{CO}(^{13}CO)$ Contours

The $N_{CO}(^{13}CO)$ contours are generated from ^{13}CO observations. The contour units are $1 \times 10^{15} \text{ cm}^{-2}$. The declination (DEC) versus right ascension (RA) plot shows the same five CO hot spots present in Figure 7 ($T_A(^{13}CO)$ Contours).

To determine $N_{CO}(^{13}CO)$, the ratio $\Delta V(^{13}CO)$ to $\Delta V(^{12}CO)$ was found to be 1.52 ± 0.04 (see Table III-Profile Half Width Ratios). The centre (0.0,0.0) is,

$$\alpha(1950) = 04^{\text{h}}26^{\text{m}}34^{\text{s}}.0 \text{ (Right Ascension)}$$

$$\delta(1950) = 35^{\circ}13'00''.0 \text{ (Declination)}$$

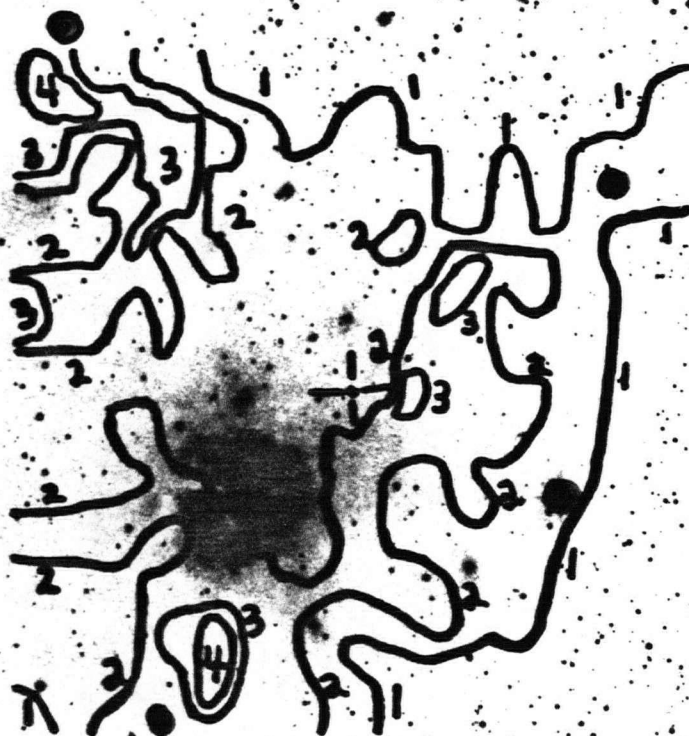


Figure 13. $(V = 5500 \text{ \AA})$, A, Extinction Contours

The magnitudes of extinction were determined using the standard procedure outlined in section III.6-Star Counting Theory, Data, and Results. The numbers on each contour map represent the interval of extinction. For example, a 4 would indicate the extinction is between 3 and 4 magnitudes. The conversion procedure is outlined in Dickman 1978. Centre (0.0,0.0),

$\alpha(1950) = 04^{\text{h}}26^{\text{m}}34^{\text{s}}.0$ (Right Ascension)

$\delta(1950) = 35^{\circ}13'00''.0$ (Declination)

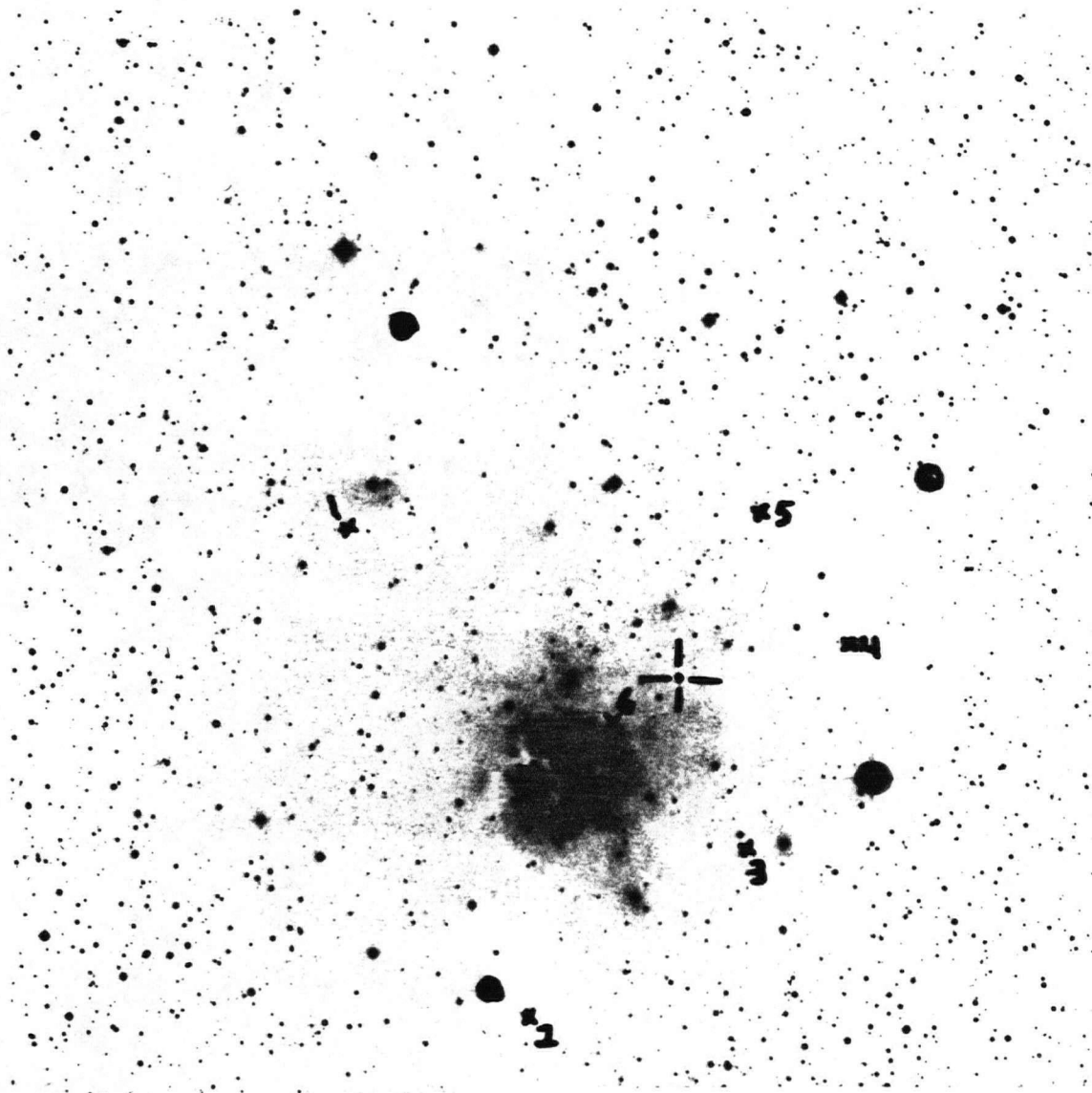


Figure 14 -Infrared Diagram

Figure 14 is a schematic representation of the infrared print (8000 to 9000 Å) sent by Dr. E. Craine of the Steward Observatory, University of Arizona, Tucson, Arizona. The converging arrows is the centre of our survey field,

$\alpha(1950) = 04^{\text{h}}26^{\text{m}}34^{\text{s}}.0$ (Right Ascension)

$\delta(1950) = 35^{\circ}13'00''.0$ (Declination)

Lk H α 101 is indicated by 10 and the other infrared stars in our observation field are numbered. The details of each are summarized in Table VII-Infrared Star Positions.



Figure 17

The contours show HI emission integrated over the velocity range -6 to $+10$ km s^{-1} . The contour steps correspond to intervals of 1.5×10^{20} cm^{-2} in column density. (Dewdney and Roger 1981).

V. CONCLUSIONS

In conclusion, Lk H α 101 is a B0.5 star. The radio core of the HII region is less than one arcsecond across with a more extended region of weaker emission out to 32 arcseconds. Visually, NGC 1579 is a five arcminute nebula surrounded by a 24 arcminute shell of weaker emission of light.

Our ^{12}CO results show a wide region of ^{12}CO emission (10 K), but the exact boundaries are as yet undetermined. The north and west boundaries have been determined. We suspect the emission extends as far as a visual extinction of one magnitude, which covers an area nearly one degree wide and several degrees in length. The average radiation temperature, T_A^* (^{12}CO), is 10 K. Within our survey field we found a large fragmented region with five hot spots of up to 20 K.

Since ^{13}CO was not observed ^{13}CO data were generated from the ^{12}CO observations. Both the ^{12}CO and ^{13}CO T_A^* contours have five hot spots within a single envelope of CO emission located southeast of Lk H α 101. CO clouds #1, Lk H α 101 (7.2, -10.8), #2, Lk H α 101 (0.0, -10.8), and #3, Lk H α 101 (7.2, -5.4) are resolved. Their masses derived from calculated ^{13}CO column densities are $49M_\odot$, $41M_\odot$, and $25M_\odot$ respectively. Two other unresolved clouds are located at Lk H α 101 (3.6, -5.4) and Lk H α 101 (0.0, -1.8). They are clouds #4 and #5 and have masses of $11M_\odot$ and $25M_\odot$. All of the fragments are embedded in the same 13 K ^{12}CO contour centered on Lk H α 101 (3.6, -7.2).

Comparing the CO data to Dewdney and Roger's (1981) HI data, we find an anticorrelation between the positions of the peak contours of the two studies. The HI contours lie to the

northwest of the CO contours. This indicates that these two different tracers are mapping separate regions. The HI velocity half width is larger than that for the ^{12}CO . The derived peak HI column densities from both tracers are $\sim 1.3 \times 10^{21}$ atoms cm^{-2} .

The visual extinction contours show a reasonable correlation between the higher A_V and CO warm regions. This is in agreement with the work of Dickman (1978) and Frerking et al. (1981). The peak HI emission occurs in regions where the visual extinction is lower than average. The exciting star has presumably been able to dissociate H_2 into HI to the northwest where A_V is lower. Dewdney and Roger (1981) have modeled this asymmetry quite well by assuming a steep discontinuity of density near Lk H α 101 to the east.

Surrounding our 13 K ^{12}CO contour are three sets of infrared stars. They are infrared stars #2, #3, and the six surrounding Lk H α 101 (Table VII). This interesting configuration agrees with the predictions of the 'Blister' model (Israel 1977, Gilmore 1978). Star formation was likely initiated on the outskirts of the cloud and has proceeded inwards. The CO hot spots we observe would be the next generation of infrared stars. Confirmation will require a more detailed mapping with better resolution of the region centered on Lk H α 101 (3.6, -7.2) and ^{13}CO observations throughout the region.

BIBLIOGRAPHY

- Allen, D.A. 1973, Monthly Notices Royal Astron. Soc. 161:1P.
- Allen, C.W. 1963, Astrophysical Quantities, University of London, London, Athlone Press.
- Altenhoff, W.J., Braes, L.L.E., Olsson, F.M., and Wendker, H.J. 1976, Astron. Astrophys. 46:11.
- Bernes, C. 1979, Astron. Astrophys. 73:67.
- Bohlin, R.C., Savage, B.D., and Drake, J.F. 1978, Ap.J. 224:132.
- Bok, B.J. 1937, "The Distribution of Stars in Space", Chicago, University of Chicago Press.
- Blitz, L., and Lada, C.J. 1979, Ap.J. 227:152.
- Braun, R. 1980, Physics 449 Directed Studies Report, University of British Columbia.
- Brown, R.L., Broderick, J.J., and Knapp, G.R. 1976, Monthly Notices Royal Astron. Soc. 175:87P.
- Bruyn, J.R. de 1979, Physics 449 Directed Studies Report, University of British Columbia.
- Cohen, M. 1980, Monthly Notices Royal Astron. Soc. 190:865.
- Cohen, M., and Dewhirst, D.W. 1970, Nature 228:1077.
- Cohen, M., and Kuhi, L.V. 1979, Ap.J. Suppl. 41:743.
- Cohen, M., and Woolf, N.J. 1971, Ap.J. 169:543.
- Craine, E. 1981, private communication (unpublished data).
- Dewdney, P.C., and Roger, R.S. 1981, private communication (unpublished data).
- Dickman, R.L. 1976, Ph.D. Dissertation, Columbia University.
- Dickman, R.L. 1978, Ap.J. Suppl. 37:407.
- Elmegreen, B.G., and Lada, C.J. 1977, Ap.J. 214:725.
- Evans II, N.J. 1981, IAU Symp. #87 page 1, Riedel Pub., Holland.
- Felli, M., and Churchwell, E. 1972, Astron. Astrophys. Suppl. 5:369.
- Frerking, M.A., Langer, W.D., and Wilson, R.W. 1981, preprint "The Relationship Between Carbon Monoxide Abundance and Visual Extinction in Interstellar Clouds."

- Gilmore, W.S. 1978, Ph.D. Dissertation, University of Maryland.
- Goldreich, P., and Kwan, J. 1974, Ap.J. 189:441.
- Grasdalen, G.L., and Gaustad, J.E. 1971, Astron.J. 76:231.
- Habing, H.J., and Israel, F.P. 1979, Annual Review Astron. Astrophys. 17:345.
- Harris, S. 1976, Monthly Notices Royal Astron. Soc. 174:601.
- Herbig, G.H. 1956, Publ. Astron. Soc. Pacific 68:353.
- Herbig, G.H. 1971, Ap.J. 169:537.
- Hobbs, P., and Shuter, W.L.H. 1981, private communication.
- Hubble, E. 1922, Ap.J. 56:162.
- Israel, F.P. 1977, Ph.D. Dissertation, University of Leiden.
- Knapp, G.R., Kuiper, T.B.H., Knapp, S.L., and Brown, R.L. 1976, Ap.J. 206:443.
- Mahoney, M.J. 1976, Ph.D. Dissertation, University of British Columbia.
- Neugebauer, G., and Leighton, R.B. 1969, Two Micron Sky Survey: A Preliminary Catalogue NASA SP-3047.
- Osterbrook, D.E. 1974, "Astrophysics of Gaseous Nebulae", San Fransisco, Freeman.
- Panagia, N. 1973, Astron.J. 78:929.
- Pease, F.G. 1917, Ap.J. 46:24.
- Penzias, A.A., Jefferts, K.B., and Wilson, R.W. 1971, Ap.J. 165:229.
- Penzias, A.A., Solomon, P.M., and Jefferts, K.B. 1972, Ap.J. 174:L43.
- Riegel, K.W. 1967, Ap.J. 148:87.
- Rhijn, P.J. van 1929, Groningen Publ. 43.
- Schwartz, P.R., and Spencer, J.H. 1977, Monthly Notices Royal Astron. Soc. 180:297.
- Sewall, J.R. 1980, Second Year Research Project, University of Maryland.
- Sharpless, S.L. 1959, Ap.J. Suppl. 4:257.

- Shuter, W.L.H., and McCutcheon, W.H. 1974, Royal Astron. Soc. Canada Jour. 68:301.
- Simon, T., and Dyck, H.M. 1977, Astron.J. 82:725.
- Spencer, J.H., and Schwartz, P.R. 1974, Ap.J. 188:L105
- Strecker, D.W., and Ney, E.P. 1974, Astron.J. 79:797.
- Szabo, A. 1980, M.Sc. Dissertation, University of British Columbia.
- Tenorio-Tagle, G. 1979, Astron. Astrophys. 71:59.
- Thompson, R.I., and Reed, M.A. 1976, Ap.J. 205:L159.
- Thompson, R.I., Erickson, E.F., Witteborn, F.C., and Strecker, D.W. 1976, Ap.J. 210:L31.
- Thompson, R.I., Strittmatter, P.A., Erickson, E.F., Witteborn, F.C., and Strecker, D.W. 1977, Ap.J. 218:170.
- Turner, B.E. 1971, Astrophys. Lett. 8:73.
- Ulich, B.L., and Haas, R.W. 1976, Ap.J. Suppl. 30:247.
- Wilson, E.W., Jefferts, K.B., and Penzias, A.A. 1970, Ap.J. 143:L161.
- Wilson, W.J., Schwartz, P.R., and Epstein, E.E. 1973, Ap.J. 183:871.
- Zuckerman, B., and Palmer, P. 1974, Annual Review Astron. Astrophys. 12:279.

APPENDIX: T_A^* (^{12}CO) CONTOURS AT CONSTANT VELOCITY

In this appendix we present T_A^* (^{12}CO) contours at constant L.S.R. velocity for the $J=1\rightarrow 0$ transition of ^{12}CO in Sharpless 222. The method of reduction is described fully in section III.3. In these figures we specify the isotope, the velocity and the contour interval (K). The contour unit was chosen to represent the average peak to peak noise for the data.

